Reviewed Preprint
v1 • April 28, 2026
Not revised

For correspondence:
hongzb@a-star.edu.sg
f.bono@exeter.ac.uk

Competing interests: No competing interests declared

Funding: See page 28

Reviewing editor: Mauricio Comas-Garcia, Universidad Autónoma de San Luis Potosí, Mexico

The structure of Egalitarian in complex with the *K10* mRNA localization signal reveals a modular binding surface required for function

Zebin Hong[1,2,5], **Li Jin**[3], **Jonas Mühle**[2,4], **Fulvia Bono**[1,2]

[1]Living Systems Institute, University of Exeter, Exeter, United Kingdom • [2]Max Planck Institute for Biology, Tübingen, Germany • [3]Cell Biology Division, MRC Laboratory of Molecular Biology, Cambridge, United Kingdom • [4]Paul Scherrer Institute, Villigen, Switzerland • [5]Institute of Molecular and Cell Biology (IMCB), Agency for Science, Technology and Research (A*STAR), Singapore, Singapore

eLife Assessment

This manuscript has **convincing** data that provides a high-resolution structure of the Egl-RNA complex. The findings are **important** to understand the formation, stability, and interactions of this complex. However, the manuscript could be improved by conducting a rigorous statistical analysis, a deeper understanding of apparent discrepancies in the stoichiometric Egl-to-RNA ratio, and exploring the specificity of this complex using a more diverse set of control RNAs.

https://doi.org/10.7554/eLife.110988.1.sa3

Abstract

Asymmetric localization of mRNAs is a prevalent mechanism for spatial control of protein function and typically involves active transport by cytoskeletal motors. The mechanisms of recognition of localizing mRNAs by motor complexes are poorly understood. Egalitarian is an adaptor protein that binds localization signals in specific RNAs in *Drosophila* and recruits them to the dynein-dynactin complex for microtubule-based transport. We determined the crystal structure of Egalitarian in complex with the localization signal of the *K10* mRNA. Three structural units of Egalitarian, a 3'-5'exonuclease domain, a linker and a C-terminal domain form shape-specific, base-directed and backbone interactions with the RNA. Based on the structure we identified conserved residues recognizing RNA *in vitro*. Genome-edited flies with mutations in these residues have deficits in Egalitarian function that are congruent with changes in *in vitro* RNA binding affinities. Our work demonstrates how a minimal RNA localization signal is recognized by an RNA localization factor.

Introduction

The localization of mRNAs to distinct cytoplasmic domains regulates many biological processes in eukaryotic cells such as embryonic patterning, cell polarity and neuronal function(Besse and Ephrussi, 2008; Holt and Bullock, 2009; Sutton and Schuman, 2006). This process is an effective way to restrict expression of proteins in cytoplasmic sub-compartments, thus spatially controlling gene expression(Martin and Ephrussi, 2009; St Johnston, 2005).

The transport of most localized mRNAs depends on cytoskeletal motors(Martin and Ephrussi, 2009; Tekotte and Davis, 2002). The localizing mRNAs are recognized by *trans*-acting protein factors that link them to microtubule-based motors. This recognition depends on *cis*-acting

elements located mainly in the 3' untranslated regions (3'UTRs) of mRNAs(St Johnston, 1995). The molecular mechanisms of how *trans*-acting factors recognize the RNA signals and link the mRNAs to the motor machinery are poorly understood.

Many mRNAs move towards the minus ends of microtubules by the dynein motor and its accessory complex, dynactin(Herbert et al., 2017; Trovisco et al., 2016; Vazquez-Pianzola et al., 2017). In *Drosophila melanogaster* the dynein-dynactin complex is involved in the localization of several essential patterning factors during early development. Dynein-dynactin-dependent transport has been described in several *Drosophila* cell types including oocytes, syncytial blastoderm embryos, neuroblasts and sensory neurons(Bullock and Ish-Horowicz, 2001; Ho et al., 2022; Hughes et al., 2004). mRNAs are linked to the dynein-dynactin machinery in these cells by the evolutionarily conserved coiled-coiled adaptor Bicaudal D (BicD) and the RNA-binding protein Egalitarian (Egl)(Bullock and Ish-Horowicz, 2001; Claussen and Suter, 2005; Dienstbier et al., 2009; Hughes et al., 2004; Mach and Lehmann, 1997; Navarro et al., 2004; Oh et al., 2000). Egl directly binds to mRNA localization elements in different mRNAs as well as the C-terminal domain (CTD) of BicD(Dienstbier et al., 2009). In addition, Egl also directly binds to the Dynein light chain (Dlc), facilitating cargo transport(Hoogenraad et al., 2001; Navarro et al., 2004) Transport complexes consisting of Egl, BicD, dynein, dynactin and mRNAs reconstituted *in vitro* are sufficient for long distance mRNA transport on microtubules(McClintock et al., 2018; Sladewski et al., 2018), revealing this is the minimal machinery for trafficking.

Minimal mRNA signals required for Egl-mediated minus-end-directed transport have been characterized in several mRNAs, including *bicoid (bcd)*, *fushi tarazu*, *gurken*, *hairy*, *fs(1)K10 (K10)*, *wingless*, and the *I Factor* retrotransposon(Bullock et al., 2003; Cohen et al., 2005, 2005; dos Santos et al., 2008; Macdonald and Kerr, 1998; Serano and Cohen, 1995; Snee et al., 2005; Van De Bor et al., 2005). These localization signals are predicted to form stem-loop structures of ~40–65 nucleotides (nt)(Bullock et al., 2003; Cohen et al., 2005, 2005; dos Santos et al., 2008; Macdonald and Kerr, 1998; Serano and Cohen, 1995; Snee et al., 2005; Van De Bor et al., 2005). As these *cis*-acting elements show little primary sequence similarity to each other, it is unclear how they are recognized by the same protein.

K10 is one of the most comprehensively studied mRNA cargoes for Egl. This mRNA is synthesized in the nurse cells and transported to the oocyte by Egl-BicD-dynein-dynactin where it is needed to establish dorso-ventral polarity of the future embryo(Cheung et al., 1992; Serano and Cohen, 1995). The 44-nucleotide transport and localization signal (TLS) of *K10* is necessary and sufficient for the localization of transcripts during early oogenesis (stage 2), late oogenesis (until stage 10) and in blastoderm embryos(Bullock and Ish-Horowicz, 2001; Serano and Cohen, 1995). Comprehensive mutagenesis of the *K10* TLS combined with injection-based localization assays in blastoderm embryos revealed that both primary and secondary structural elements are important for recognition by the transport machinery(Bullock et al., 2010).

The molecular details of how Egl recognizes the *K10* TLS or other RNA-localization elements are currently unknown. Egl is a 1004-amino-acid protein predicted to include a large uncharacterized N-terminal region, a 3'-5' exonuclease (EXO) domain from the DEDDy superfamily and a C-terminal part containing a short consensus Dlc-binding region(Dienstbier et al., 2009; Mach and Lehmann, 1997; Navarro et al., 2004). Biochemical assays revealed that a large N-terminal portion of the protein encompassing the EXO domain is able to bind RNA(Dienstbier et al., 2009).

Here, we present the X-ray crystal structure of the minimal RNA-binding region of Egl in complex with the *K10* TLS. The structure reveals that RNA recognition is mediated by the EXO domain, a small positively charged domain and a helical linker separating these elements. Egl recognises the *K10* TLS by a combination of shape and sequence-specific interactions suggesting a mechanism for mRNA target discrimination. Editing of the *egl* locus in *Drosophila* using CRISPR/Cas9 shows that the residues involved in RNA recognition are essential for *in vivo* function, thus validating the structure.

Results

The central region of Egl is sufficient for RNA binding *in vitro*

Based on sequence analysis, three main conserved regions can be identified in Egl (Figure 1A; Figure S1A). The N-terminal region (Egl^{N}, residues 1-500) includes an uncharacterized domain that bears the minimal binding region for BicD (BicD-BR, residues 1-79; (Dienstbier et al., 2009)), which links the RNP complex to dynein-dynactin(Dienstbier et al., 2009; Liu et al., 2013; Mach and Lehmann, 1997; Navarro et al., 2004). The central region of Egl (Egl^{MID}, residues 500-850) is predicted to include a 3'-to-5' exonuclease domain (EXO) that is essential for RNA-binding *in vitro* (Dienstbier et al., 2009), followed by a small domain predicted to contain helical features. The C-terminal portion of Egl (Egl^{C}; residues 850-1004) is uncharacterized apart from and a short Dynein light chain-binding motif (Dlc-BM)(Hoogenraad et al., 2001; Navarro et al., 2004). Previous analysis of RNA binding *in vitro* showed that a protein encompassing Egl^{N} and Egl^{Mid} (Egl^{1-819}) is sufficient for specific recognition of mRNA signals *in vitro*(Dienstbier et al., 2009).

To further define the boundaries of the Egl RNA-binding region, we produced a series of truncations (Figure 1A), and measured binding affinities to the *K10* TLS by Fluorescence Anisotropy (FA). After confirming that the presence of a GST tag does not affect binding of $Egl^{512-819}$ to RNA significantly in control experiments (Figure S1B), each Egl variant was purified as a GST fusion to improve solubility and enhance FA sensitivity. All truncated versions of Egl bind to *K10* TLS in the sub-micromolar range, similar to Egl^{1-819} (Figure 1B-D), revealing that $Egl^{512-819}$ is sufficient for full RNA binding. Including regions of the C-terminus ($Egl^{512-1004}$) did not significantly affect RNA binding (Figure 1B-D). Thus, we conclude that $Egl^{512-819}$ is sufficient to bind to *K10* TLS *in vitro*.

The $Egl^{512-819}$ -*K10* TLS complex is stable and monomeric in solution

To understand the molecular mechanisms of Egl recognition of *K10* TLS, we first reconstituted a minimal complex *in vitro* using $Egl^{512-819}$. We added two G-C-pairs at the base of the *K10* TLS stem that have been shown to stabilize the structure in solution and showed no loss of *in vivo* localization (Bullock et al., 2010). The RNA-protein complex is stable as shown by size-exclusion chromatography (SEC) and elutes as a well-defined peak with a larger elution volume compared with that of apo $Egl^{512-819}$ (Figure 1E). Both $Egl^{512-819}$ alone and in complex with *K10* TLS eluted with an elution volume consistent with that of a monomer. This result was also confirmed by SEC coupled to right-angle light scattering (SEC-RALS) that showed that $Egl^{512-819}$ alone or in complex with *K10* TLS is monomeric in solution and binds to *K10* TLS with a 1:1 protein-RNA stoichiometry (Figure S1E-F).

Overview of the structure of $Egl^{512-819}$ in complex with *K10* TLS

We obtained crystals of the SEC-purified complex of $Egl^{512-819}$-*K10* TLS. The structure was determined by molecular replacement (MR) at 3.1-Å resolution (Table 1) using a model generated by I-TASSER based on a homologous template, RNAse D(Barbosa et al., 2014). The crystal lattice includes two complexes of $Egl^{512-819}$-*K10* TLS in the asymmetric unit (ASU). The two complexes superimpose with root mean square deviation (RMSD) of 0.634 Å over 1971 atoms. The crystal contact interface between them is stabilized through hydrogen bonds and salt bridges (Figure S2A-C).

In the final $Egl^{512-819}$ model, the C-terminal region of the construct is not visible (aa 769-819) and several loop regions (aa 512-519, 552-553, 652-655, 720-723) are disordered and could not be modeled (Figure 2A-B). In the *K10* RNA model, the loop from A20 to C27 ($loop^{R}$) is not well defined and was also not modeled. The C-terminal part of the protein contains a region that we termed the Egl helical domain (EHD). To further study the EHD that could not be modeled unambiguously, we generated a construct encoding residues 743 to 819 of Egl (Linker (L)-EHD)

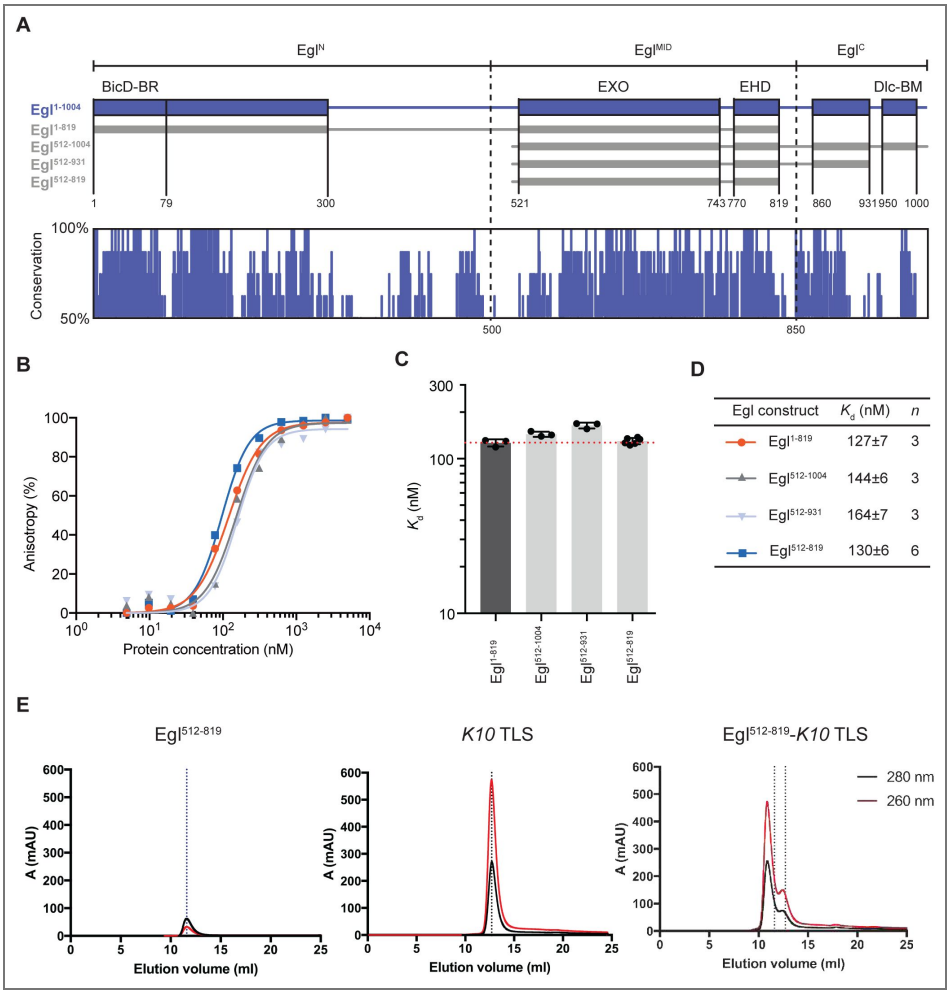

Figure 1. Egl$^{512-819}$ is sufficient for RNA binding.

(A) Schematic representation of the architecture of full-length Egl and the truncated constructs used. Solid boxes represent domains predicted to be folded, while lines are regions predicted to be unstructured. A conservation plot based on the alignment of multiple Egl homologs is shown below (Scores based on Consurf(Ashkenazy et al., 2016)). Sequences used to generate the alignment plot are shown in Figure S1. In the plot, residues positions are represented in the x-axis and percent identities (50-100%) are indicated in the y-axis. **(B)** K_d values were determined by FA. 5'-FAM-labeled *K10* TLS was incubated with increasing concentrations of Egl constructs and the data were fitted to the Hill equation to obtain the K_d. **(C)** Column graph with mean K_d values shown as bars, standard deviation as black error bars and individual measurements as black dots. Data are represented as mean ± standard deviation (SD). **(D)** Table of the *K10* TLS RNA binding affinities to various Egl truncations. *n* is the number of independent measurements. **(E)** SEC profiles of purified Egl$^{512-819}$ (left), *K10* TLS alone (middle) and Egl$^{512-819}$ preincubated with a 1.2-fold excess of *K10* TLS (right). The positions of the peaks are indicated by dotted lines in different shades of gray: the elution volume of Egl$^{512-819}$ in isolation is in blue, while that of *K10* TLS RNA is in black

Table 1. **Data collection and refinement statistics of the crystal structures of Egl$^{512-819}$-*K10* TLS complex and of MBP- (GSAM)- L-EHD and of *K10*-TR.**

Data collection			
Crystal	Egl$^{512-819}$-*K10* TLS	MBP-Egl$^{743-819}$	*K10*-TR
Wavelength (Å)	1.0000	1.0000	0.9999
Space group	*P*212121	*P*212121	*P*41212
a, *b*, *c* (Å)	68.90, 107.40, 140.80	52.80, 82.00, 120.20	70.20, 70.20, 81.30
α, *β*, *γ* (°)	90, 90, 90	90, 90, 90	90, 90, 90
Resolution (Å)	50-3.08 (3.27-3.08)	50-2.20 (2.34-2.20)	50-3.60 (3.82-3.60)
R_{meas}	0.17 (1.41)	0.12 (1.37)	0.31 (1.29)
$I/\sigma I$	8.07 (1.55)	8.10 (1.01)	5.29 (1.57)
Completeness (%)	99.8 (99.1)	99.2 (98.7)	99.7 (98.9)
Redundancy	7.02 (7.10)	3.08 (3.08)	6.21 (6.24)
No. unique reflections	36673 (5931)	50894 (8163)	4519 (731)
CC(1/2)	0.999 (0.702)	0.996 (0.354)	0.992 (0.928)
Refinement			
R-factor	0.2402	0.1933	0.2914
R-free	0.2916	0.2059	0.2990
Average B value (Å^2)	117.00	54.77	
No. atoms			
Protein	5828	3330	-
RNA	1642	-	874
Ligand/ion	8	23	-
Water	-	-	-
R.m.s. deviations			
Bond lengths (Å)	0.014	0.016	0.004
Bond angles (°)	2.026	2.028	0.860
Ramachandran plot (MolProbity)			
Favored (%)	92.99	97.64	-
Allowed (%)	7.01	2.36	-
Outliers (%)	0	00	-

Statistics for the highest-resolution shell are shown in parentheses. Molprobity was used for validation.

fused to the Maltose Binding Protein (MBP) as a crystallization driver (Figure 2A). We crystallized and determined the crystal structure of MBP-L-EHD at 2.5-Å resolution by MR using MBP as a search model (Table 1). The obtained electron density is well defined and allowed us to model residues 743 to 806 with confidence (Figure 2C; Figure S2D). The final Egl$^{512–819}$–K10 TLS model was obtained by superimposing the two crystal structures using the shared rigid helical linker (L) as the alignment reference (Figure 2E).

The overall structure of Egl$^{512-819}$ consists of an N-terminal EXO domain and the small, positively charged EHD connected by a helical linker (Figure 2E; Figure S2D). *K10* TLS forms a typical A-form dsRNA duplex with an overall conformation similar to ideal A-form dsRNA (RMSD 3.1 Å over 40 nucleotides) (Figure S3; Table 1). In the complex, RNA base pairing is mostly by Watson-Crick interactions with the exception of a wobble base pair (between G6-U43) and two bulges at C35 and A41 named Bulge1 and 2, respectively (Figure 3B). In the structure, Bulge2 lies on the opposite face of the helix to Bulge1, thus pointing to solvent and not interacting directly with the protein. Therefore, when in complex with Egl$^{512-819}$, Bulge2 of *K10* TLS is in a similar structural position compared with *in silico* predictions (mFold;(Zuker, 2003)). However, it differs from the conformation of unbound *K10* TLS in solution, where Bulge2 is spatially arranged on the same side of the RNA stem as Bulge1 and involves nucleotide A39 (Figure S3;(Bullock et al., 2010)). Conversely, in the complex, Bulge2 consists of A41. Conformational flexibility could explain the less kinked conformation of the stem loop in the complex as compared with the previous NMR structure of *K10* TLS(Bullock et al., 2010). The folding of *K10* TLS in the complex is similar to a partial crystal structure we obtained of unbound *K10 TLS* that shows A-form conformation (Figure S3; Table 1).

The interaction surface of Egl$^{512-819}$ with *K10* TLS covers 905.7 Å^2. Similarly, the *K10* TLS interaction surface involved in binding Egl$^{512-819}$ is 1175.2 Å^2. In the structure of the Egl$^{512-819}$-*K10* TLS complex, the first 3'-most five nucleotides and the last 5' complementary five at nt 44-48 associate tightly with the EXO domain (Figure 2E and 3; Figure S2D). The region that spans from nt C35 to A37, located around Bulge1, forms contacts with both linker and EHD. Interactions in this region are charged, and occur mostly with the RNA phosphate backbone (Figure 2D and 3).

The EXO domain adopts a typical α/β fold, consisting of a six-stranded β-sheet flanked by α-helices. A structure-based search using the DALI server(Holm and Laakso, 2016) identified several EXO domain-containing proteins including *E. coli* RNase D, *T. brucei* RRP6 and *B. mori* Exonuclease 3'-5' domain-containing protein 1 (Exd1) (Figure S4A). Among these, RNase D shares the highest structural similarity with the EXO domain of Egl (RMSD 2.255 Å over 670 atoms) albeit with low sequence identity (21%) (Figure S4A). Based on structural comparisons, and as predicted by previous sequence analysis ((Navarro et al., 2004)Moser et al., 1997; Figure S1), the EXO domain of Egl belongs to the DEDDy superfamily. The conserved signature of DEDDy proteins are the catalytic tetrad and a tyrosine in so-called motif III. The EXO domain of Egl contains the four highly conserved acidic residues Asp561, Glu563, Asp621, and Asp708, and also the tyrosine (Tyr704) in motif III (Figure S1). The close arrangement of these residues in the Egl structure is consistent with the EXO domain of Egl retaining 3'-5' exonuclease activity. However, mutation of all five putative catalytic residues does not affect RNA binding and *in vivo* function(Dienstbier et al., 2009; Navarro et al., 2004).

The EHD domain is composed of two positively charged α-helices facing each other in antiparallel arrangement and connected by unstructured loops (helix-loop-helix). Both helices contact the linker helix of Egl while helix α14 contacts the middle and upper regions of the RNA stem around bulge 1 (Figure 2E and 3). No significant structural homology of the EHD to known domains/motifs was retrieved upon databases searches but this could be due to its small size.

A 35 Å long helical linker connects the EXO and EHD domain, which is also highly positively charged. A comparison between Egl$^{512-819}$-*K10* and the L-EHD structures shows that the linker is in a fixed position relative to the EXO and EHD domains and superposes with an RMSD of 1.031 Å over 117 atoms (Figure 2). Indeed, the linker position is stabilized by several hydrophobic and salt bridges interactions with EHD and EXO domain residues (Figure 2 and S4B).

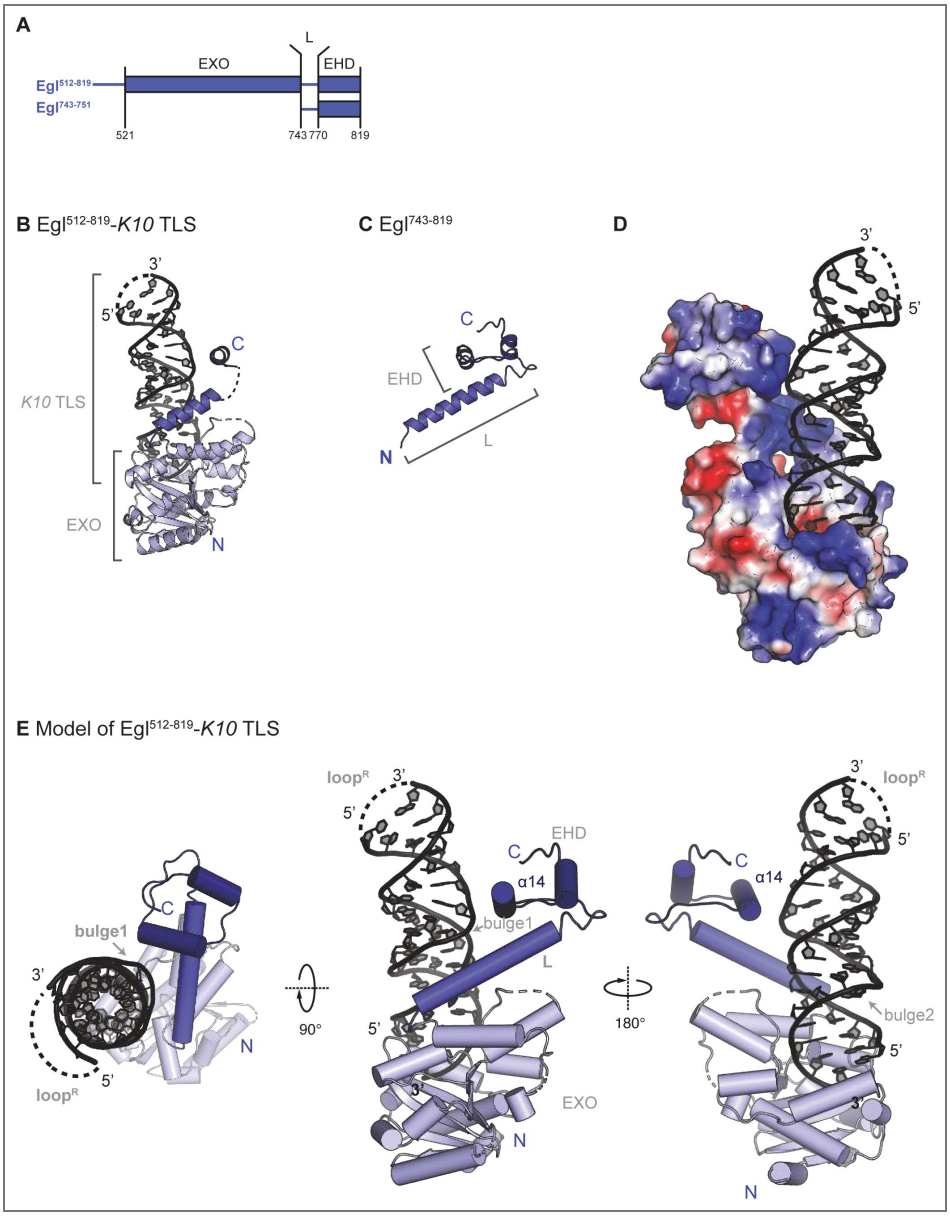

Figure 2. Structure of the Egl$^{512-819}$-*K10* TLS complex.

(A) Schematic representation of the Egl truncated constructs using for structural studies. **(B)** Crystal structure of Egl$^{512-819}$ (with incomplete L and EHD regions) in complex with *K10* TLS. **(C)** Crystal structure of L-EHD. **(D)** Electrostatic potential plotted on the surface of Egl$^{512-819}$ with a gradient from red (negative) to blue (positive) from – to +5K *T/e*, respectively. **(E)** Model of Egl$^{512-819}$ in complex with *K10* TLS in three different views related by 90° and 180° rotation. The model is obtained by superposition of the structures in **(B)** and **(C)**. The structures are shown as cartoon with Egl and *K10* TLS colored in a gradient in blue and black, respectively.

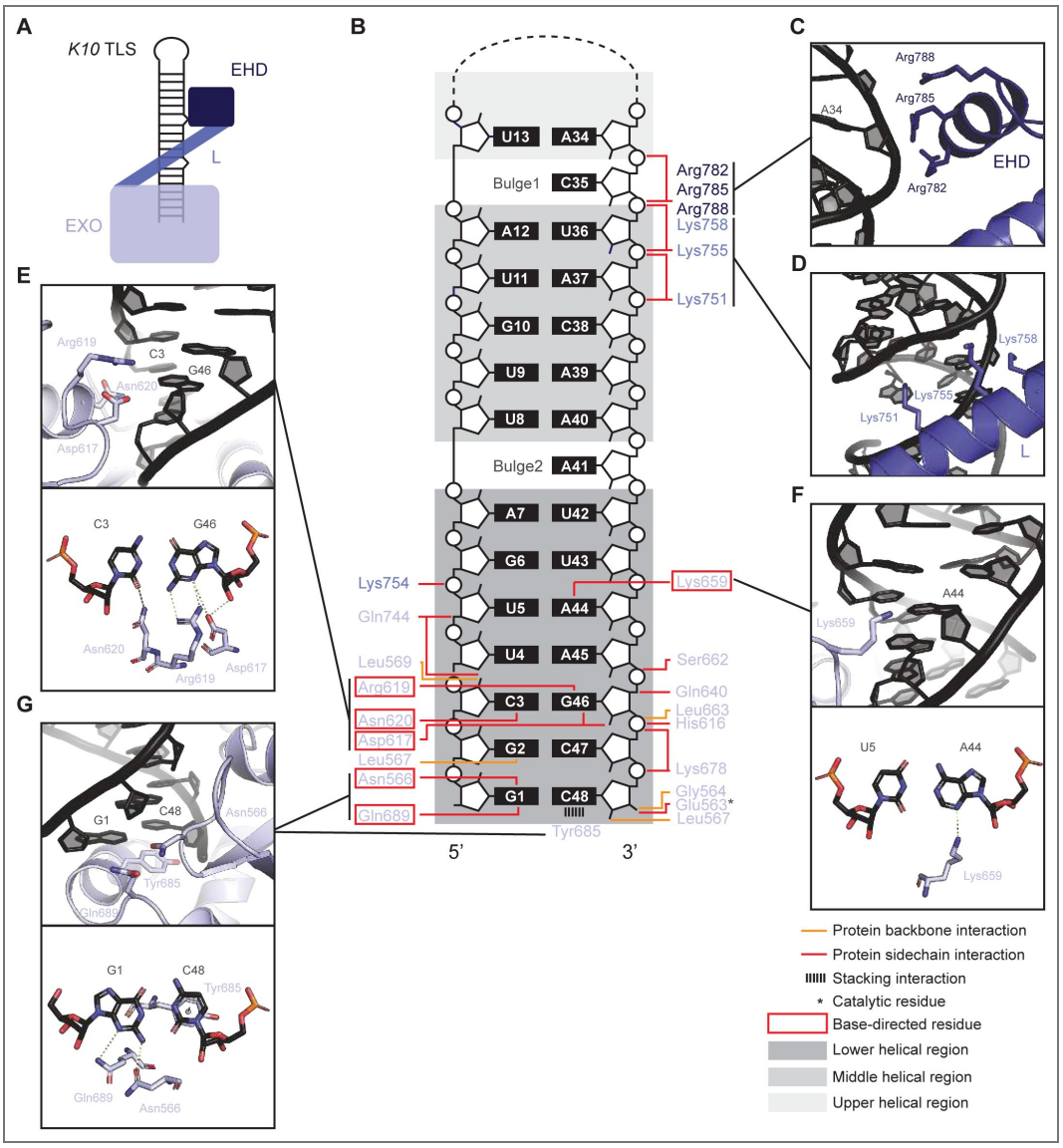

Figure 3. **Protein-RNA interactions within the Egl$^{512-819}$-*K10* TLS complex.**

(A) Schematic representation of the architecture of Egl$^{512-819}$-*K10* TLS complex. Egl$^{512-819}$ recognizes the *K10* TLS with several contacts in the EXO, Linker and EHD. **(B)** Schematic representation of the interactions between Egl$^{512-819}$ and *K10* TLS. **(C-H)** The zoom-in panels show residues involved in the RNA binding. In **(C-H)**, Egl$^{512-819}$ and *K10* TLS are shown as cartoon, and the figures in **(A-G)** share the same color-coding.

Protein-RNA interactions within the Egl$^{512-819}$-*K10* TLS complex

The association between Egl$^{512-819}$ and the *K10* TLS RNA is mainly driven by electrostatic interactions. Positively charged residues are concentrated at the RNA interface (Figure 2D; Figure S4C). These positively charged residues are conserved in evolution (Figure S4D), supporting an important functional role.

The EXO domain clasps the lower part of *K10* TLS mainly by unspecific sugar- and phosphate-backbone interactions but also with a few direct base recognitions (Figure 3). The Watson-Crick base pairs G1-C48 and C3-G46 as well as A44 are involved in base-directed recognition. The side chains of Asn566 and Gln689 form hydrogen bonds with G1 and the aromatic side chain of Tyr685 is π-stacked against the 3'-terminal C48 (Figure 3G; Figure S2D). This interaction occurs with the first of the two RNA stabilizing G-C pairs we added to the sequence and involves a 3'OH base-specific recognition. However, the natural base pair predicted to form the base of the RNA stem is C-G, which would also be engaged in a similar and specific recognition in the absence of the artificial G-C doublet.

In addition, the conserved residues Asp617, Arg619 and Asn620 recognise the third base pair C3-G46 through hydrogen bonding interactions (Figure 3E). A direct interaction is also observed between Lys659 and A44 (Figure 3F). The nonspecific contacts between the Egl$^{512-819}$ EXO domain and the RNA backbone can be divided into three groups: those forming hydrogen bonds with O2' of the phosphate moiety (Gln744, Leu569 and Leu567), those forming hydrogen bonds or salt bridges with phosphate groups (Glu563, Lys678, Ser662, Leu663, His616, Gly564 and Glu563), and hydrophobic interactions with the sugar backbone (Gln640 and Gln744) (Figure 3B). Of the five putative catalytic residues only Glu563 interacts directly with the 3'-OH of the RNA backbone.

In the mid region of the RNA stem, four positively charged residues (Lys751, Lys754, Lys755 and Lys758) in the linker of Egl$^{512-819}$ (Figure 3D) and three (Arg782, Arg785 and Arg788) in the EHD (Figure 3C) are in close contact with the negatively charged RNA backbone. Although there are no base-specific contacts in this region, the phosphate-backbone interaction in correspondence with Bulge1 at C35 is involved in electrostatic interactions with conserved positively charged amino acids and might play an important role in Egl substrate selectivity through a shape preference. There are no contacts between Egl$^{512-819}$ and the upper region of *K10* TLS that include the upper stem and loop.

Conserved residues of Egl$^{512-819}$ are involved in RNA binding

The Egl EXO domain, linker and EHD domain all contact the *K10* TLS. To investigate the individual contribution of each region to RNA binding, we first generated a series of truncated versions of Egl that included the EXO domain (EXO, Egl$^{512-751}$), EXO and linker (EXO-L, Egl$^{512-770}$), and linker and EHD (L-EHD, Egl$^{743-819}$) (Figure 4A) and measured binding affinities to 5'-6-carboxy-fluorescein (6-FAM)-labelled *K10* TLS by FA. The linker and EHD could not be purified separately and were not used for affinity measurements.

The affinity of the Egl EXO domain for *K*10 TLS is at least 50 times lower than that of Egl$^{512-819}$ as no binding up to 5 μM RNA could be detected. In contrast, L-EHD bound with a K_d of 262 ± 9 nM, only two-fold weaker than Egl$^{512-819}$ (Figure 4C-E). To examine the role of the linker region, we extended the EXO construct to include the linker. This EXO-L construct binds in the high nanomolar range with a K_d of 807 ± 104 nM, suggesting that the linker contributes to RNA binding and that the EHD acts as effector of RNA binding (Figure 4C-E). Overall, these results indicate that Egl EXO domain, linker and EHD domain all contribute to binding, consistent with the structure.

To identify key residues involved in RNA-binding, we selected 16 conserved residues on each region for alanine scanning mutagenesis (Figure 4B). All mutants exhibit circular dichroism (CD) spectra similar to that of Egl$^{512-819}$ wild type (wt), indicating that mutants are properly folded (Figure S5A). Most individual Ala mutations reduce the affinity to *K10* TLS only up to two-fold (Figure S5B-C). Next, to disrupt salt bridges we individually replaced all of the positively

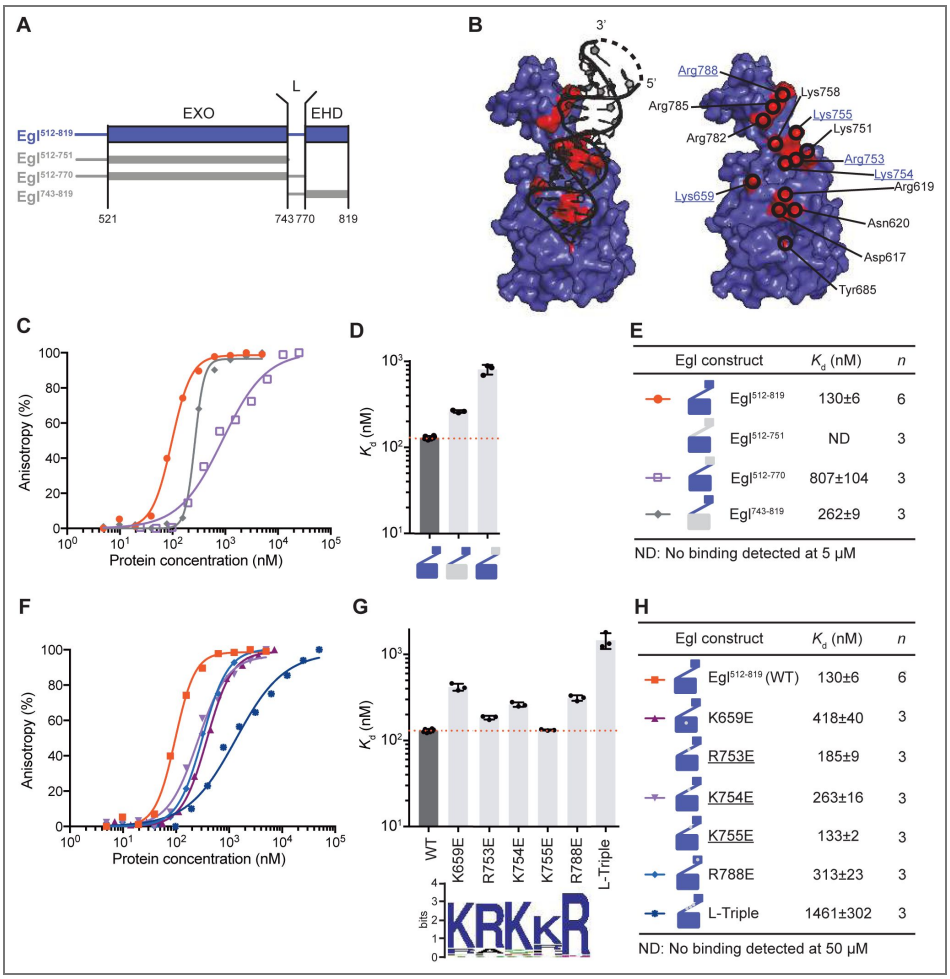

Figure 4. Mutagenesis analysis on the residues of Egl$^{512-819}$ involved in RNA binding.

(A) Schematic representation of the Egl truncated constructs. **(B)** The residues of Egl involved in the binding of *K10* TLS are highlighted in red and labeled on the protein surface rendering. On the right side, interacting residues are labelled. Underlined in blue are conserved residues mutated in the assays. **(C)** and **(F)** K_d values were determined by FA. 5'-FAM-labeled *K10* TLS was incubated with increasing concentrations of Egl mutants and the data were fitted to the Hill equation to obtain the K_d. Data are represented as mean ± SD. **(D)** and **(G)** Column graph with mean K_d was shown as bars in the same color-coding, standard deviation as black error bars and individual K_d values as black dots. Weblogo representation of the residues involved in RNA binding was shown below the column graph. **(E)** and **(H)** K_d values of Egl mutants for *K10* TLS are shown in the table ±SD.

charged residues by Glu. These reverse-charge mutants had either a similar or slightly stronger effect than the respective Ala mutants with an up to a 3-fold reduction in affinity (Figure 4F-H). Next, we tried to combine single mutations to more strongly impair RNA binding. Three combinations (D617A/R619A/N620A, R753E/K754E/K755E and K659E/K754E/R788E) were selected for measurements. Asp617, Arg619 and Asn620 form base-directed hydrogen bonds with the base pair C3-G46 (Figure 3A). The D617A/R619A/N620A triple mutant shows two-fold reduction in binding with a K_d of 273 ± 12 nM (Figure S5B-C). These residues are all located on the EXO domain and their mutation reduces binding affinity to a similar degree as the EXO-domain deletion. This result confirms the contribution of the EXO domain to RNA binding and reveals residues that functionally contribute to RNA binding. The next triple mutant we tested disrupts a positively charged patch (Arg753, Lys754 and Lys755) in the linker region (L-Triple). This mutant shows a ten-fold reduction in binding affinity (1461 ± 302 nM) (Figure 4F-H). Finally, we combined mutations affecting each domain (EXO, K659E; linker, K745E; EHD, R788E). We did not detect RNA binding for this triple mutant (Figure S5B-C).

Determinants of RNA shape and sequence for Egl binding

To test the specificity of Egl$^{512\text{-}819}$ binding towards RNA targets, we first measured direct binding affinity to different FAM-labeled RNA oligomers by FA. However, with this method, we could not detect large differences in affinities between Egl$^{512\text{-}819}$ and various target and non-target RNAs (Figure S6A-C). As an alternative approach, we set up a competition assay in which the preformed Egl$^{512\text{-}819}$-FAM *K10* complex was incubated with increasing amounts of various unlabeled RNAs.

Previous work suggested that RNA secondary structure is important for specific recognition by Egl(Bullock et al., 2003; Bullock and Ish-Horowicz, 2001; Claussen and Suter, 2005; Hughes et al., 2004; Mach and Lehmann, 1997; Navarro et al., 2004; Oh et al., 2000). To test this, we measured the half-maximal inhibitory concentration (IC_{50}) against single-stranded RNA (ssRNA), double-stranded RNA (dsRNA) and a non-target stem loop RNA derived from a bacteriophage (*MS2*) (Figure 5A-C and S6D). ssRNA was a weak competitor of *K10* TLS for Egl$^{512\text{-}819}$ binding with an IC_{50} of 112 ± 19 μM, which is 2000-fold weaker than control competitor *K10* TLS. In contrast, dsRNA and *MS2* stem loop are two-fold weaker competitors than *K10* TLS (Figure 5A-C). Thus, a double helix is required for efficient competition with *K10* TLS. We also tested both ssDNA and dsDNA. As expected, dsDNA was a much weaker competition compared to dsRNA. ssDNA competition could not be detected even at a 40,000-fold excess over *K10* TLS (Figure 5A-C).

As controls for the assay, we included another Egl target, *bcd* stem-loop 5 (*bcd*_VbL;(Lazzaretti et al., 2016)) and an Egl-independent dsRNA element from the human *ARF1* transcript(Kim et al., 2005) (Figure 5D-F and S6D). *bcd*_VbL competed very efficiently with *K10* RNA, whereas *ARF1* RNA was a 1.9-fold weaker competitor.

In the structure we observed five base-directed interactions involving the G1-C48 pair, the C3-G46 pair, and A44. We focused on the G1-C48 pair because its substitution to an AU pair removes one hydrogen bond to Egl. This leads to a small but consistent (1.2-fold) reduction in competition. The structure also revealed an interaction of Egl to a bulge at C35. We inserted the bulge on the opposite strand in the same position. This *K10*-b1as RNA also showed a mild reduction in competition. When we combined the two substitutions, we found an additive effect on competition with a 1.6-fold reduction. This RNA species competes similarly to the antisense *K10* RNA, an RNA that is unable to localize in an Egl-dependent manner *in vivo*(Dienstbier et al., 2009) (Figure 5D-F). Deletion of both bulges (*K10*-Δb1b2) also leads to defects in *in vivo* localization and to a 1.2-fold reduction in competition(Bullock et al., 2010).

The addition of native 10 nt flanking sequence of the RNA (*K10*-flank) and the addition of the two stabilizing base pairs, as used for structure determination (*K10*-2GC) at the base of the stem did not alter competitive ability as compared to *K10* TLS (Figure 5D-F), this aligns with previous *in vivo* findings showing that such G–C substitutions do not disrupt K10 mRNA localization. In summary, specific interactions involving both sequence-specific and shape recognition contribute to

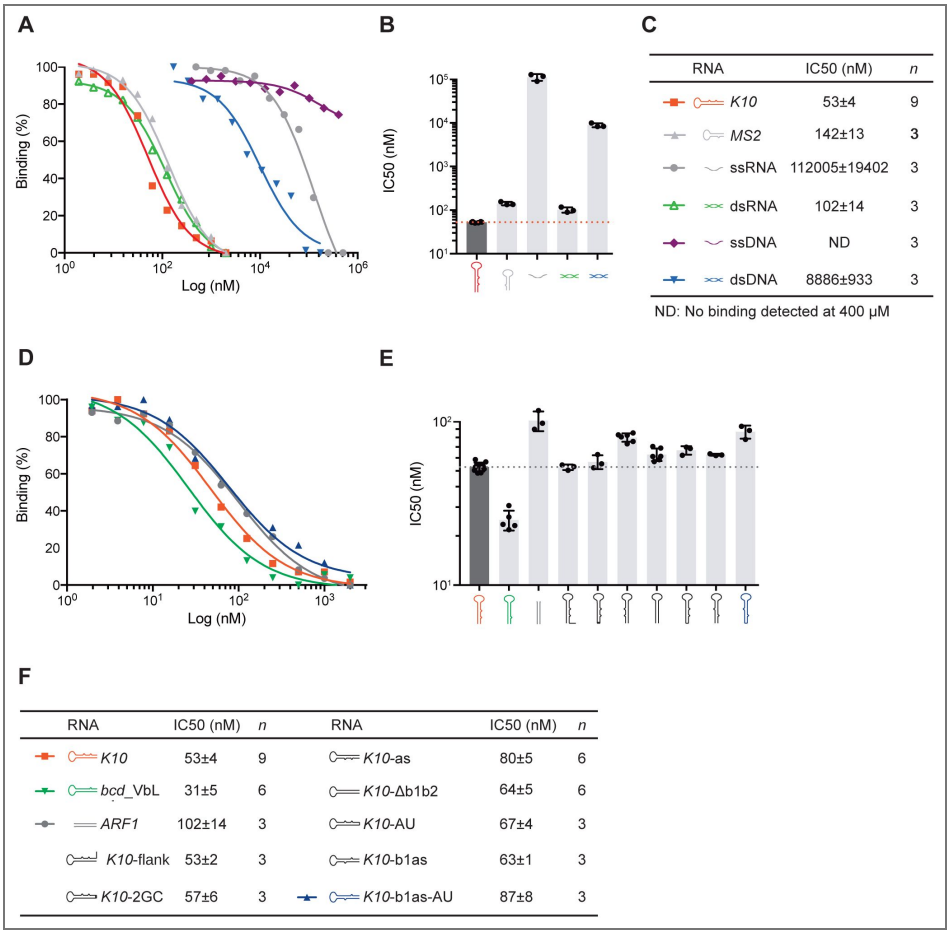

Figure 5. **RNA binding specificity of Egl$^{512-819}$.**

(A) and **(D)**, Egl$^{512-819}$ was preincubated with 5'-FAM-labeled *K10* TLS RNA and unlabeled RNAs before measurement. The change in anisotropy was plotted and fitted to sigmoidal curve to obtain the IC_{50}. (**B**) and (**E**), Column graph with mean IC_{50} was shown as bars, standard deviation as black error bars and individual IC_{50} values as black dots. **(C)** and **(F)**, IC_{50} values of unlabeled RNAs are shown in the table. Data are represented as mean ± SD.

preference of Egl for different RNA targets. Some of the mutations with a small effect on *in vitro* competition have a large effect on Egl-dependent *in vivo* localization. We cannot exclude the possibility that other cellular components contribute to *in vivo* target selection by Egl.

RNA binding is required for Egl function *in vivo*

We next evaluated the *in vivo* significance of RNA-protein interactions defined by our structure. We first used CRISPR/Cas9-mediated homology directed repair ((Port et al., 2014); Figure S7A) to create an allele of the endogenous *Drosophila egl* gene coding for a protein with the R753E, K754E and K755E mutations in the linker ($egl^{L\text{-}triple}$). As described above, the wild-type residues contact in *K10* TLS and the presence of all three mutations lowers the affinity of $Egl^{512\text{-}819}$ for the *K10 TLS in vitro* by approximately one order of magnitude (Figure 4F-H).

Null mutations in *egl* have been described previously, and are most commonly associated with premature termination of translation. Flies homozygous for these alleles survive to adulthood but females are infertile. These females lack eggs due to a failure to differentiate an oocyte(Carpenter, 1994; Mach and Lehmann, 1997; Theurkauf et al., 1993). Homozygous mutant $egl^{L\text{-}triple}$ females were also infertile and had a complete absence of egg production (Figure 6A). Immunostaining of ovarioles for a marker of the oocyte (Orb; (Lantz and Schedl, 1994)) and the synaptonemal complex (Corolla;(Page and Hawley, 2001) revealed the $egl^{L\text{-}triple}$mutation, like previously existing *egl* null mutations, prevented differentiation of the oocyte within the germarium (Figure 6B). An indistinguishable phenotype was observed in ovarioles of $egl^{L\text{-}triple/}egl^{null}$ females (Figure 6B). The finding that the phenotype associated with the $egl^{L\text{-}triple}$ allele was not complemented by an egl^{null} chromosome generated in an independent study reveals that the phenotype is not due to an off-target mutation. Immunostaining of egg chambers with an antibody that specifically recognises Egl(Mach and Lehmann, 1997) showed that the $egl^{L\text{-}triple}$mutation does not destabilise the Egl protein (Figure S7). Collectively, these observations reveal that the $egl^{L\text{-}triple}$ mutation strongly disrupts the function of the Egl protein *in vivo*.

To further examine the physiological relevance of our *in vitro* results, we used the same CRISPR methodology to introduce the K659E mutation into Egl (Figure 6C). As described above, K659 resides in EXO domain and contacts A44 of the *K10 TLS* in the crystal structure. K659E lowers the affinity of $Egl^{512\text{-}819}$ for the *K10 TLS in vitro*, although to a lesser degree than the triple mutation R753E/K754E/K755E (~3-fold vs ~10-fold (Figure 4)). Females homozygous for the *K659E* mutation were fertile and exhibited no overt defects in oogenesis (Figure 6C and D). $egl^{K659E/}egl^{null}$females were also fertile. However, ~30% of early egg chambers from these animals did not restrict the oocyte marker to a single cell, whereas ~20% did not enrich the synaptonemal complex marker in a single cell (Figure 6C and D). These observations indicate a failure to specify or maintain an oocyte in a subset of cases. There was no overt decrease in Egl protein levels in the mutant egg chambers (Figure S7). Collectively, these data show that K659E partially disrupts the function of the Egl protein *in vivo*.

In summary, our phenotypic analysis reveals that the RNA binding residues in $Egl^{512\text{-}819}$ are also important for the function of the full length Egl protein *in vivo.* The correlation between the extent to which the mutations we tested inhibit RNA binding *in vitro* and the degree of disruption of oocyte differentiation *in vivo* further supports the physiological relevance of our *in vitro* studies.

Discussion

Here, we solved the X-ray crystal structure of the RNA-binding region of Egl in complex with the *K10* transport and localization signal (TLS). The structure revealed how Egl recognizes the *K10* TLS by a combination of shape and sequence-specific interactions. Our structure-based *in vivo* mutagenesis in *Drosophila* showed that key residues involved in *K10* TLS recognition are also important for *in vivo* function.

The EXO domain of Egl contains the conserved signature of DEDDy proteins consisting of five highly conserved residues (Figure S1 and S4) and shares the highest structural similarity with RNase D. RNase D is an active 3' to 5' DEDDy-group exonuclease with a function in the maturation

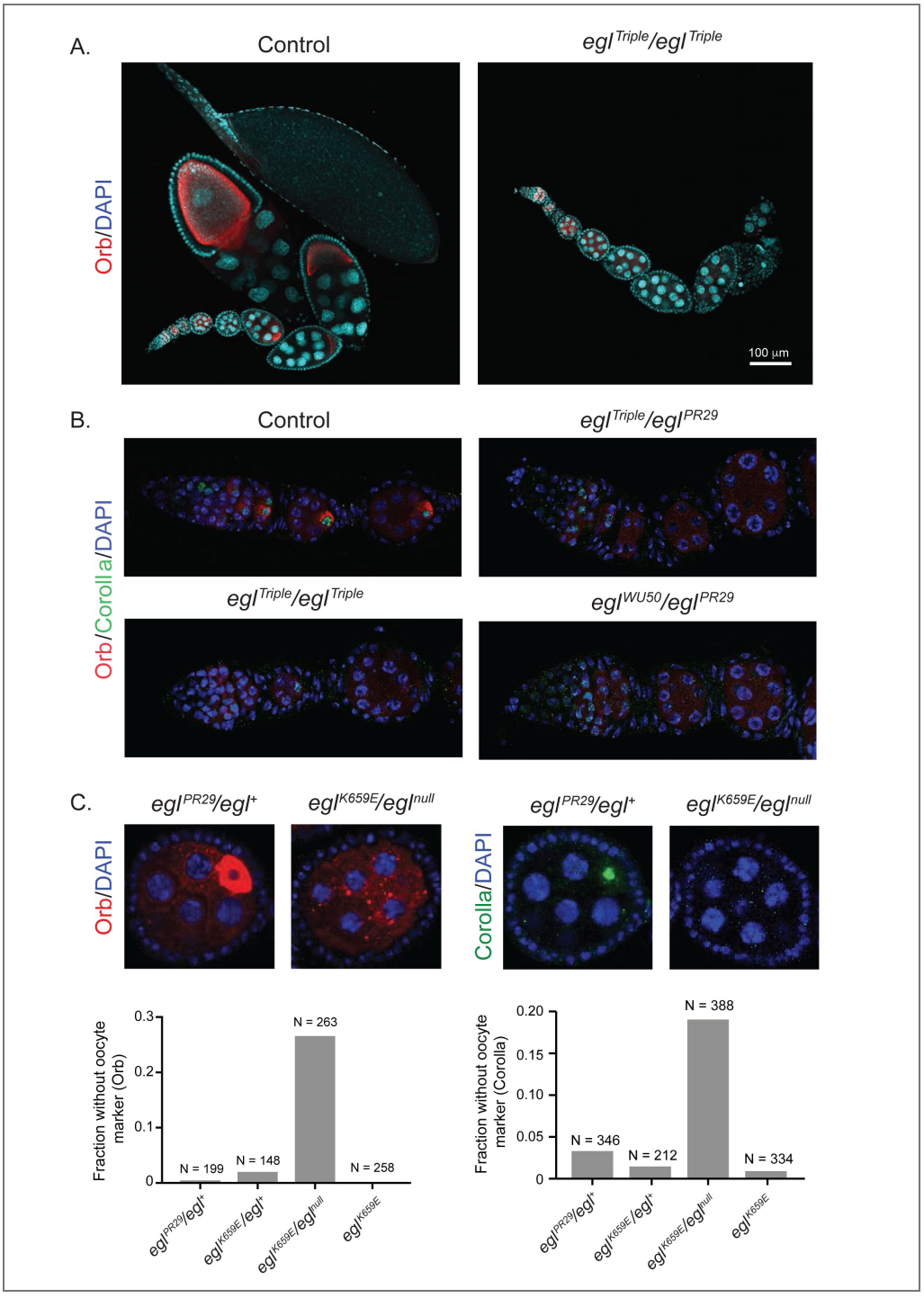

Figure 6. Egl residues required for RNA binding *in vitro* are required for function *in vivo*.

(A) Images of germaria and early-stage egg chambers for the indicated genotypes stained for the oocyte markers Orb (red; cytoplasmic marker) and Corolla (green; marker of the meiotic synaptonemal complex), as well as DNA (blue; DAPI). Arrowheads label oocytes in the control. In each of the mutant genotypes, all egg chambers fail to differentiate an oocyte (images are representative of at least 200 ovarioles visualized per genotype). *PR29* and *WU50* are previously characterized *egl* null alleles(Mach and Lehmann, 1997). **(B)** Left: stage 4/5 egg chambers of the indicated genotypes stained for Orb, Corolla and DNA, illustrating the partially penetrant oocyte differentiation defect in *K659E/PR29* ovarioles. Right: quantification of oocyte differentiation phenotypes in the indicated genotypes (oocytes scored using Orb immunostaining; n = number of egg chambers examined). Control genotypes in the images in A and B are *L-Triple/+* and *PR29/+*, which had phenotypes indistinguishable from the wild-type. Scale bars in A and B = 20 µm.

of RNAs(Li et al., 1998). Our structural analysis of Egl reveals that the DEDDy residues are appropriately positioned with respect to each other in a putative catalytic centre. Remarkably, mutations of the active site residues do not affect binding to mRNA localization signals and the *in vivo* function during oogenesis(Dienstbier et al., 2009; Navarro et al., 2004). The evolutionary conservation of the DEDDy motif indicates that Egl may have exonuclease activity that contributes to other aspects of its function. However, Egl's major function in mRNA localization appears to have evolved in parallel to the exonucleolytic activity.

The origin of new RNA-binding proteins from enzymes involved in RNA metabolism seems to have occurred repeatedly in evolution(Lazzaretti et al., 2016). For example, the RNA-binding protein Exuperantia (Exu) binds RNA by a modified exonuclease-like domain and a SAM domain. The exonuclease active-site is lost in *Drosophila* Exu but is present in some mollusc and vertebrate Exu homologs(Lazzaretti et al., 2016). Another example is Exd1, a mammalian protein related to Egl that recruits small RNAs in the piRNA pathway through its inactive exonuclease-like domain(Yang et al., 2016). In Egl, RNA binds around the catalytic site and a positively charged surface formed by the helical linker and the EHD domain. In Exu, RNA-binding has been mapped by MS cross-linking and also localizes to a patch around the active site and the SAM domain(Lazzaretti et al., 2016). In both Egl and Exu, novel RNA-binding activity may have evolved by the addition of positively charged surfaces to stabilize the interactions between the RNA substrate and the exonuclease.

Previous biochemical and single-molecule imaging studies indicate that two Egl molecules form a complex with one mRNA containing a single stem-loop structure(McClintock et al., 2018; Sladewski et al., 2018). In our SEC-RALS experiment and crystal structure, the minimal RNA-binding region of Egl binds to *K10* TLS with a 1:1 stoichiometry. This difference could be due to the shorter RNA or truncated Egl used in our study. It is unclear how two molecules of full-length Egl can bind to an mRNA with one stem loop. In our structure, we identified weak interactions between two Egl molecules in the asymmetric unit. These or other parts of Egl lacking from our structure may contribute to the formation of a 2:1 Egl-mRNA complex. In addition, the two Egl molecules may bind to different surfaces of the RNA stem loop. In our structure, both Egl molecules bind to both *K10* TLS stem loops. The second interaction site has a much smaller interaction surface with the RNA. This weak interaction or interactions to neighbouring ssRNA might recruit a second molecule of Egl to the mRNA. Our structural work paves the way for understanding higher order RNA-protein interactions in the transported RNP.

Our crystal structure and *in vitro* affinity measurements provided insight into how Egl recognizes a specific localization element. Although Egl is also able to bind to ssRNA, dsRNA and other stem-loop RNA structures, the affinity of binding was higher for *K10* TLS. This suggests that Egl can discriminate RNA secondary structure and shows some sequence specificity. Several lines of evidence indicate that *in vivo* Egl binds stem-loop structures with bulges in localizing RNAs. First, the *K10* TLS is required for Egl binding and localization of the full-length mRNA (Cohen papers, Bullock 2001; 2010). Second, several mRNAs that depend on Egl for minus-end-directed transport during oogenesis and embryogenesis have similar predicted structures containing bulged regions(Bullock et al., 2010, 2003; Cohen et al., 2005; dos Santos et al., 2008; Macdonald and Kerr, 1998; Serano and Cohen, 1995; Snee et al., 2005; Van De Bor et al., 2005).

The Egl-*K10* TLS structure and our biochemical and *in vivo* experiments revealed the structural details and relevance of Egl-stem-loop interactions. We identified specific interactions between Egl and *K10*-TLS-Bulge1 that create a unique electrostatic signature for protein recognition. The importance of bulges in stem-loop elements has also been described for other RNA-protein interactions(Hermann and Patel, 2000). In the genomic RNA of HIV-1 there are bulged adenine residues that provide recognition sites for viral proteins(Ennifar et al., 1999). These interactions depend on the secondary structure or shape of the RNAs, rather than their primary sequence. Mutation of the residues in Egl that mediate interactions to Bulge1 render Egl unable to exert its function in *Drosophila* oogenesis. In addition, there are also residues of Egl that mediate base-directed interactions and backbone interactions to the stem of the RNA stem-loop. Mutations of

these residues also reduced binding and *in vivo* function. These results indicate that the recognition of stem-loop structures is due to a combination of base- and shape-specific interactions.

Methods

Protein expression and purification

To produce the Egl protein for crystallization and FA, Egl from *D. melanogaster* was cloned into a pET-MCN vector(Diebold et al., 2011) with an N-terminal glutathione S-transferase (GST) tag followed by a TEV protease cleavage site. Mutants and truncations were generated by site-directed mutagenesis.

GST-Egl constructs were expressed *E. coli* BL21 (*DE3*) Gold (Life Technologies) cells in TB medium at 37 °C until an OD600 of 0.6-0.8 and induced at 20 °C with 0.5 mM IPTG overnight. Cells were harvested (5000 x g, 20 min, 4 °C), resuspended in buffer A (20 mM Tris-HCl, pH 7.5, 1 M NaCl, 10% glycerol, 1 mM DTT), and lysed by homogenization. The lysate was cleared by centrifugation (18000 x g, 1 hour, 4 °C), and the supernatant was incubated with Glutathione Agarose 4B resin (Macherey-Nagel). Bound protein was washed with buffer A and buffer B (20 mM Tris-HCl, pH 7.5, 300 mM NaCl, 10% glycerol, 1 mM DTT), eluted with buffer C (20 mM Tris-HCl, pH 7.5, 300 mM NaCl, 10% glycerol, 1 mM DTT, 50 mM reduced glutathione). The protein was applied to Heparin HP Column (GE Healthcare), eluted with a gradient from 300 mM to 1 M NaCl and further purified by SEC on a HiLoad 16/600 Superdex 200 pg column (GE Healthcare) in buffer B.

The $Egl^{512-819}$ construct was expressed and purified as described above, except that the GST-tag was removed by TEV protease overnight at 4 °C. The $Egl^{512-819}$-*K10* TLS complex was assembled by incubating $Egl^{512-819}$ with a 1.2-M excess of *K10* TLS on ice overnight and further purified by SEC on a HiLoad 16/600 Superdex 200 pg column (GE Healthcare) in buffer B.

The MBP- (GSAM)- L-EHD ($Egl^{743-819}$) construct was expressed *E. coli* BL21 (*DE3*) Gold (Life Technologies) cells in autoinduction ZY medium at 37 °C until OD_{600} = 2.0, and induced at 20 °C overnight. Cells were harvested and lysed as described above. The supernatant was incubated with Amylose Resin (NEB). Bound protein was washed with buffer A and buffer B (20 mM Tris-HCl, pH 7.5, 300 mM NaCl, 10% glycerol, 1 mM DTT), eluted with buffer D (20 mM Tris-HCl, pH 7.5, 300 mM NaCl, 10% glycerol, 1 mM DTT, 50 mM Maltose) and further purified by SEC on a HiLoad 16/600 Superdex 200 pg column (GE Healthcare) in buffer E (20 mM Tris-HCl, pH 7.5, 150 mM NaCl, 1 mM DTT, 10 mM Maltose).

Crystallization, data collection and analysis

Crystallization conditions were initially screened at 4°C and at 20°C using a Mosquito nanodrop dispenser (TTP Labtech) in 96-well sitting-drop plates with 100 nl protein plus 100 nl reservoir. Crystals of $Egl^{512-819}$-*K10* TLS complex grew in 50 mM sodium citrate, pH 4.8, 30% (w/v) MPD, 10 mM $CaCl_2$, 2.5 mM Spermine at 20 °C. For X-ray data collection, a single crystal was harvested without cryoprotectant and flash cooled in liquid nitrogen. Diffraction data were collected at Beamline PXII of the Swiss Light Source. The diffraction data were indexed, integrated, and scaled using the XDS program package(Kabsch, 2010). A weak molecular replacement solution [TFZ=8.4] was obtained by using a trimmed poly-Ala model (RNAse D, PDB ID: 4NLB) generated by I-TASSER(Yang and Zhang, 2015). The model building of $Egl^{512-819}$ was performed with MR-Rosetta(Terwilliger et al., 2012) and manual building in COOT(Emsley et al., 2010), and the model of *K10* TLS was built using Brickworx(Chojnowski et al., 2015) and manual run in COOT(Emsley et al., 2010). Refinement was carried out in Refmac5 using TLS and jelly body(Vagin et al., 2004).

Crystals of MBP- (GSAM)- L-EHD grew in 100 mM Tris-HCl, pH 7.5, 18% (w/v) PEG 6000, 50 mM $MgCl_2$ at 4 °C. For X-ray data collection, a single crystal was transferred to a cryoprotectant solution with mother liquor supplemented with addition of 20% glycerol, and flash cooled in liquid nitrogen. Diffraction data were collected and processed as described above. The structure was solved by molecular replacement with PHASER(McCoy et al., 2007) using the structure of

maltose binding protein (PDB ID: 1ANF)(Quiocho et al., 1997) as the search model. All subsequent model building was performed in COOT(Emsley et al., 2010) and restrained refinement in Phenix(Terwilliger et al., 2012).

Protein structure figures were generated using PyMOL (Schrödinger, LLC.). The quality of the final models was validated with the wwPDB Validation Server (*https://validate-rcsb.wwpdb.org/*). Interaction surfaces were calculated with PISA(Krissinel and Henrick, 2007).

Fluorescence anisotropy

For direct binding assay, measurements were carried out using an Infinite F200 plate reader (Tecan) at 20°C. 5'-6-FAM-labeled RNA was added to each reaction at a fixed concentration of 10 nM with different concentrations of purified Egl truncations or mutants in 50 µl buffer F (20 mM HEPES-NaOH pH 7.5, 100 mM NaCl, 10% Glycerol). Each titration point was measured three times, with an integration time of 40 µs, with 485 nm and 535 nm as the excitation and emission wavelength, respectively. The data were analyzed using the Hill equation with the Prism 6 software (GraphPad).

For competition binding assay, 150 nM $Egl^{512-819}$ was preincubated with 10 nM 5'-FAM-labeled *K10* TLS RNA for 10 min at 20°C and further incubated with different concentrations of unlabeled RNAs for 10 min at 20°C in 50 µl buffer F before measurement. The change of anisotropy was plotted and fitted to sigmoidal curve to obtain the IC_{50} with Prism 6 (GraphPad).

The sequences of the RNA and DNA oligonucleotides (Integrated DNA Technologies) are shown as follows (5' to 3'): *K10* (CUUGAUUGUAUUUUUAAAUUAAUUCUUAAAAACUACAAAUUAAG); *K10*-Δbulges (CUUGAUUGUAUUUUUAAAUUAAUUCUUAAAAAUACAAUUAAG); *K10*-antisense (GAAUUAAACAUCAAAAAUUCUUAAUUAAAUUUUUAUGUUAGUUC); *K10*-anti-C35 (CUUGAUUGUACUUUUUAAAUUAAUUCUUAAAAAUACAAAUUAAG); *K10*-AU (AUUGAUUGUAUUUUUAAAUUAAUUCUUAAAAACUACAAAUUAAU); *K10*-anti-C35-AU (AUUGAUUGUACUUUUUAAAUUAAUUCUUAAAAAUACAAAUUAAU); *K10*-2GC (GGCUUGAUUGUAUUUUUAAAUUAAUUCUUAAAAACUACAAAUUAAGCC); *K10*-flank (CUUGAUUGUAUUUUUAAAUUAAUUCUUAAAAACUACAAAUUAAGAUCACUCUGU); *ARF1* sense (dsRNA sense) (UGAGUGCCAGAAGCUGCCUC); *ARF1* antisense (GAGGCAGUUUCUGGUACUCA); dsRNA antisense (GAGGCAGCUUCUGGCACUCA); ssRNA (polyU20) (UUUUUUUUUUUUUUUUUUUU); ssRNA (polyAU20) (AUAUAUAUAUAUAUAUAUAU); *bcd*_Vb (long) (GGGCCCAAAA UGAAAAAUGUUUCUCUUGGGCGUAAUCUCAUACAAUGAUUACCC UUAAAGAUCGAACAUUUAAACAAUAAUAUUUGGG); *bcd*_Vb (short) (AAAUGUUUCUCUUGGGCGUAAUCUCAUACAAUGAUUACCCUUAAAGAUCGAACA UUU); *SOLE* (CGAUAUCGAGCAUCAAGAGUGAAUAUCG); ssDNA (dsDNA sense) (AGGCAGTTTCTGGTACTCAG); dsDNA antisense (CTGAGTACCAGAAACTGCCT); *MS2* (ACAUGAGGAUUACCCAUGU).

Right angle light scattering (RALS)

Samples were loaded onto a Superdex 75 5/150 column (GE Healthcare) connected to a TDA302 detector array (Viscotek), in buffer B at room temperature. Chromatography runs were performed with 2 mg/ml of purified Egl alone, or pre-incubated with a 1.1-M excess of *K10* TLS on ice for 10 min. The sample volume was 20 µl. Data were analyzed with OmniSEC 4.5 software.

Analytical size-exclusion chromatography

$Egl^{512-819}$ (32 uM, 500 ul) alone, or pre-incubated with a 1.2-M excess of *K10* TLS were loaded on a Superdex 75 10/300 GL column (GE Healthcare) in buffer B, and UV absorbance was monitored at 280 and 260 nm.

Circular dichroism

CD spectroscopy was performed on a JASCO-810 CD system. Wavelength scans were averages of five scans between 200 nm and 250 nm collected at 20°C in a quartz cuvette with a 1-mm path length with 0.2 mg/ml protein in buffer B.

Generation of *Drosophila egl* alleles by CRISPR/Cas9-mediated homology-directed repair

We used our previously reported CRISPR/Cas9 methodology(Port et al., 2014) to produce *egl* alleles encoding proteins with mutations of specific RNA-binding residues. Briefly, single-stranded oligonucleotide donors coding for the desired mutations (Ultramers, IDT; 500 ng/µl) were injected into the posterior of embryos that had a *nos-cas9* transgene(Port et al., 2014) (CFD2) and a transgene (integrated at attP40) that expresses a single guide (sg)RNA targeting the *egl* locus adjacent to the region to be repaired by the respective donor (embryos were generated by crossing *nos-cas9* females with sgRNA males). Spacer sequences for the two sgRNAs ($sgRNA^{L\text{-}Triple}$ and $sgRNA^{K659E}$) had previously been cloned via complementary oligonucleotides into the transformation vector pCFD3(Port et al., 2014), which expresses sgRNA from the *U6:3* promotor. CRISPR RGEN tools (*http://www.rgenome.net/*) revealed the selected sgRNAs have no other predicted targets in the *Drosophila* genome. Following injection of the donor into the transgenic embryos, flies heterozygous for the desired mutation were identified by Sanger sequencing of PCR products, as described previously(Port and Bullock, 2016). Sequences of spacer and donor oligos, as well as oligos used for sequencing the targeted region, are provided in Table S1. Balanced mutant stocks were established from the offspring of positive animals, followed by generation of homozygous females for phenotypic analysis.

Immunostaining of ovarioles

Ovarioles were dissected in PBS with 0.5% Tween (PBT0.5) and fixed in 4% paraformaldehyde/PBT0.5 for 20 minutes. Following washing in PBT0.5 (3 x 5 min and 4 x 15 min), samples were blocked in 20% Western Blocking Reagent (Roche)/PBT0.5 (Blocking Buffer) for 1 h. The following primary antibodies were then used overnight at 4°C in Blocking Buffer: (1) a combination of mouse anti-Orb (mixture of clones 4H8 and 6H4(Lantz et al., 1994) (Developmental Studies Hybridoma Bank; each diluted 1:200)) and rabbit anti-Corolla(Collins et al., 2014) (gift of Scott Hawley, Stowers Institute (diluted 1:2000)), or (2) rabbit anti-Egl (Mach and Lehmann, 1997)(gift of Ruth Lehmann, Skirball Institute; diluted 1:3000)). Following 3 x 5 min and 4 x 15 min PBT0.5 washes, secondary antibodies in Blocking Buffer (Alexa488-conjugated donkey-anti-rabbit (Life Technologies (A21206)); Alexa555-conjugated donkey-anti-mouse (Life Technologies (A31570) (each diluted 1:500)) were added for 2 h at room temperature. Washing steps were repeated and, after 2 brief washes in PBS, ovarioles were mounted in Vectashield containing DAPI (VectorLabs). Ovarioles were imaged with a Zeiss 780 confocal microscope using a Zeiss 40 x 1.3NA oil objective (except for Figure S7A (Zeiss 20 x 0.8NA objective)).

Supplementary figures

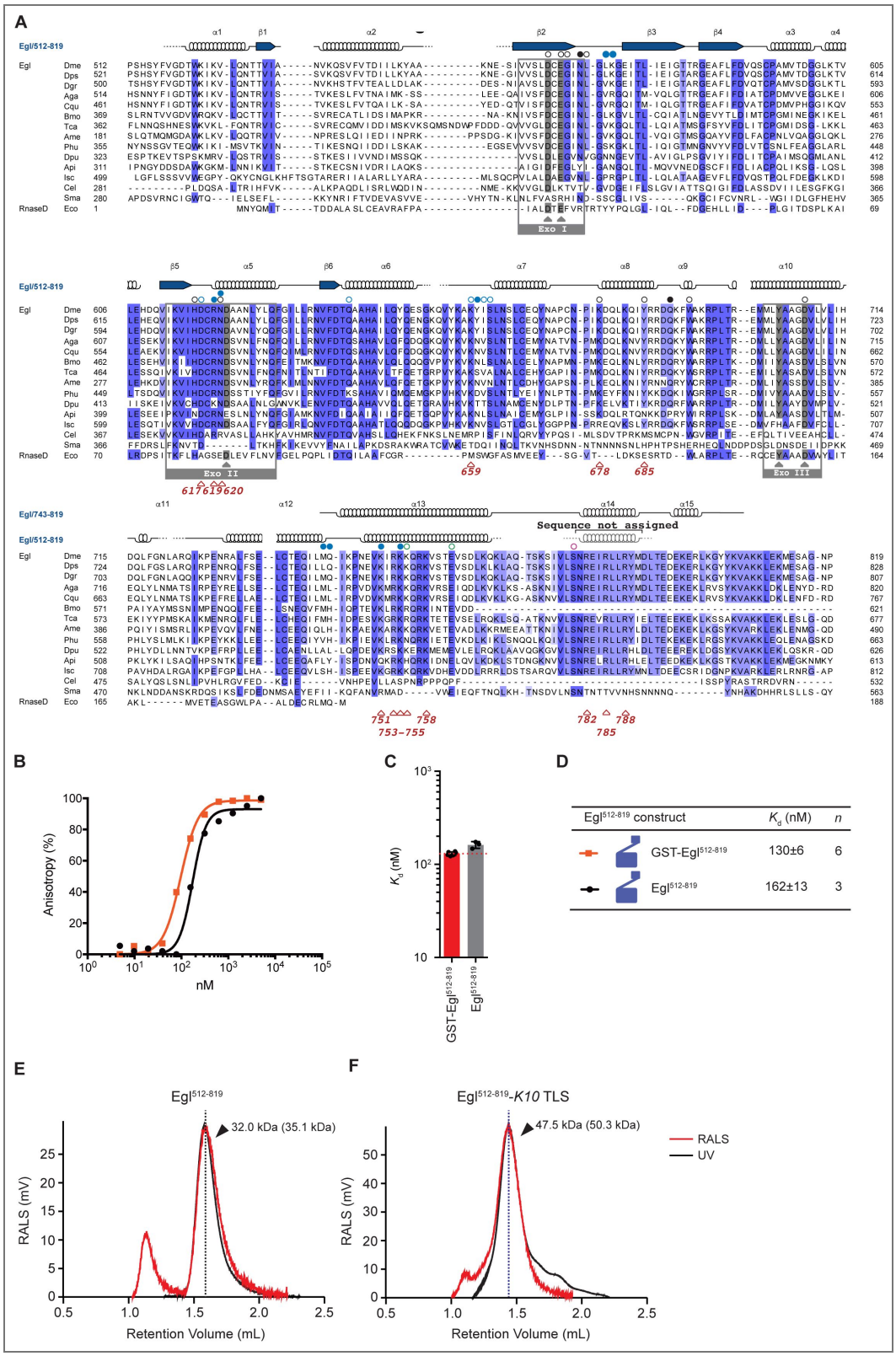

Figure S1. Alignment of Egl homologs and Egl RNA binding region, related to Figure 1. (A) Sequences used to generate the alignment include: [Insecta, order Diptera] *D. melanogaster* (Dme), *D. sechellia*, *D. simulans*, *D. erecta*, *D. yakuba*, *D. ananassae*, *D. persimilis*, *D. pseudoobscura pseudoobscura*, *D. willistoni*, *D. virilis*, *D. mojavensis*, *D. grimshawi*, *A. gambiae* (Aga), *C. quinquefasciatus*; [Lepidoptera] *B. mori* (Bmo), *H. melpomene*, *D. plexippus*;

[Coleoptera] *T. castaneum* (Tca); [Hymenoptera] *A. cephalotes*, *A. mellifera* (Ame); [Phthiraptera] *P. humanus corporis*; [Hemiptera] *A. pisum* (Api); [Crustacea] *D. pulex* (Dpu); [Chelicerata] *I. scapularis* (Ixo); [Nematoda] *C. elegans* (Cgi), *C. briggsae*, *P. pacificus*; [Plathyelmintes] *S. mansoni* (Dre); [Echinodermata] *S. purpuratus*. Numbering refers to the Dme sequence. The secondary structure of Dme Egl$^{512\text{-}819}$ and L-EHD is schematized above the alignment (beta-sheets:  ; alpha-helices:  ; residues not ordered in the structure are shown as dotted lines; gaps indicate regions for which no structural information is available). Residues interacting with the 5' or 3' strand of the *K10* stem-loop RNA are marked with a filled or with an empty dot above the Dme sequence, respectively; conserved residues are highlighted in blue according to 80% sequence identity in Jalview(Waterhouse et al., 2009). Catalytic residues in the exonuclease domain:  ; mutated residues:  ; conserved catalytic residues are highlighted in gray. The alignment was generated with MUSCLE(Edgar, 2004), visualized with Jalview (Waterhouse et al., 2009) and edited in Adobe Illustrator. **(B)** RNA binding properties of GST-tagged and untagged Egl$^{512\text{-}819}$. K_d values were determined by FA. 5'-FAM-labeled *K10* TLS was incubated with increasing concentrations of GST-Egl$^{512\text{-}819}$ or Egl$^{512\text{-}819}$ and the data were fitted to the Hill equation to obtain the K_d. Data are represented as mean ± SD. **(C)** Column graph with mean K_d was shown as bars in the same color-coding, standard deviation as black error bars and individual K_d values as black dots. **(D)** K_d values of GST-Egl$^{512\text{-}819}$ or Egl$^{512\text{-}819}$ for *K10* TLS are shown in the table ±SD. RALS profiles of Egl$^{512\text{-}819}$ unbound **(E)** and in complex with *K10* TLS RNA **(F)**. For each plot, the calculated molecular weight (MW) at the peak is indicated in black; the predicted molecular weight is shown in parenthesis. RALS and UV curves are colored in red and black, respectively.

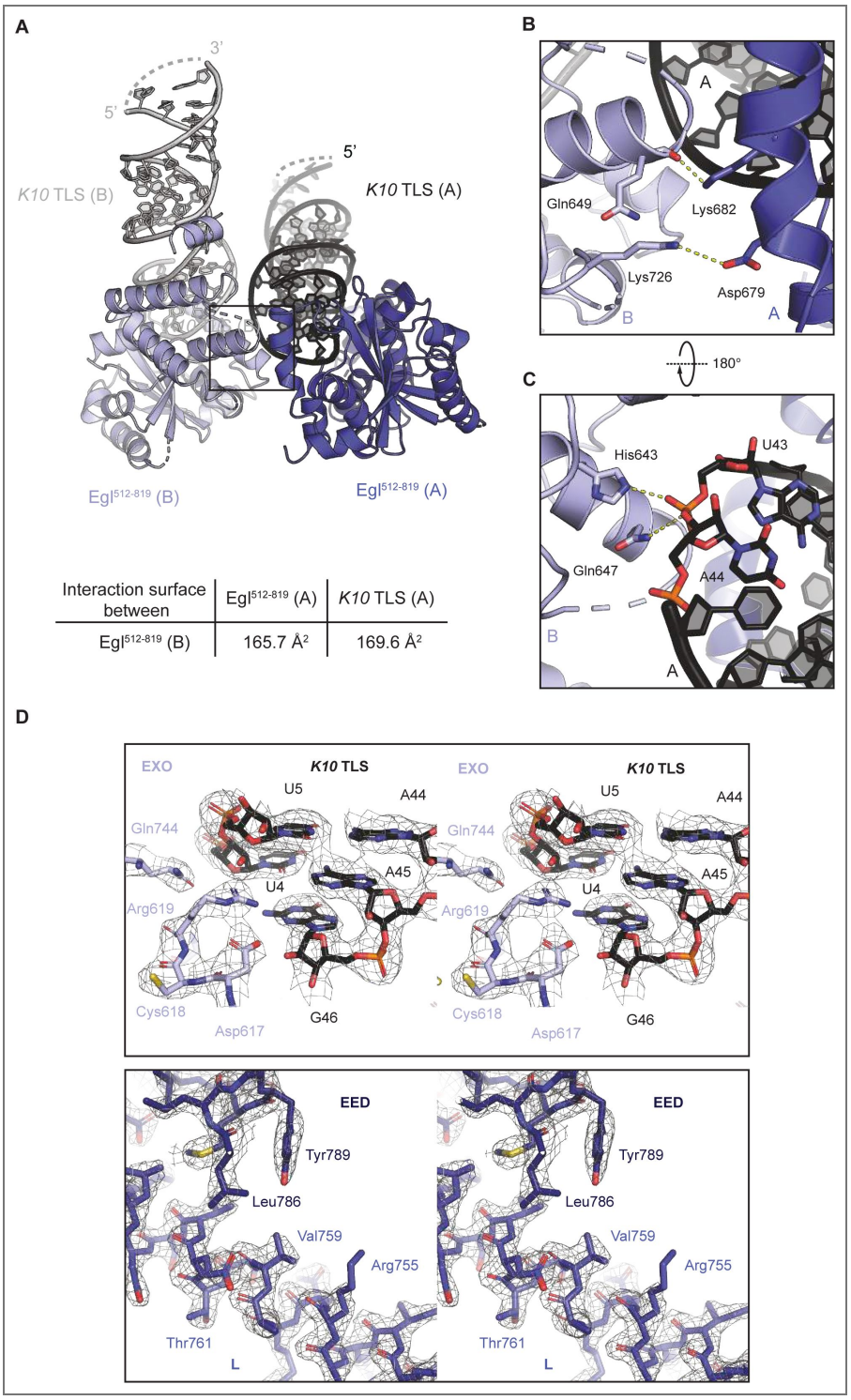

Interaction surface between	Egl$^{512-819}$ (A)	*K10* TLS (A)
Egl$^{512-819}$ (B)	165.7 Å^2	169.6 Å^2

Figure S2. Egl$^{512-819}$ multimerization state in the complex and quality of the electron density, related to Figure 2.

(A) The crystal lattice of Egl$^{512-819}$-*K10* TLS includes two complexes in the ASU. In molecule A, Egl$^{512-819}$ is rendered as cartoon in blue, while *K10* RNA is in black. In molecule B, the protein is in light blue and the RNA in gray. A table displaying the extension of the interface between the two complexes in the ASU is shown below. **(B)** A zoomed in view of the interactions at the interface between Egl$^{512-819}$ molecule A and Egl$^{512-819}$ molecule B. The side chain of Lys682^A interacts with the backbone carboxyl of Gln649 ^{B}. **(C)** Interactions between Egl$^{512-819}$ molecule B and *K10* TLS molecule A. *K10* TLS RNA^A backbone contacts His643^B and Gln647^B. With the exception of Lys726, all other interacting residues are evolutionarily conserved. **(D)** Stereo view of the electron density of the 2Fo-DFc maps for Egl$^{512-819}$-*K10* TLS complex structures after refinement.

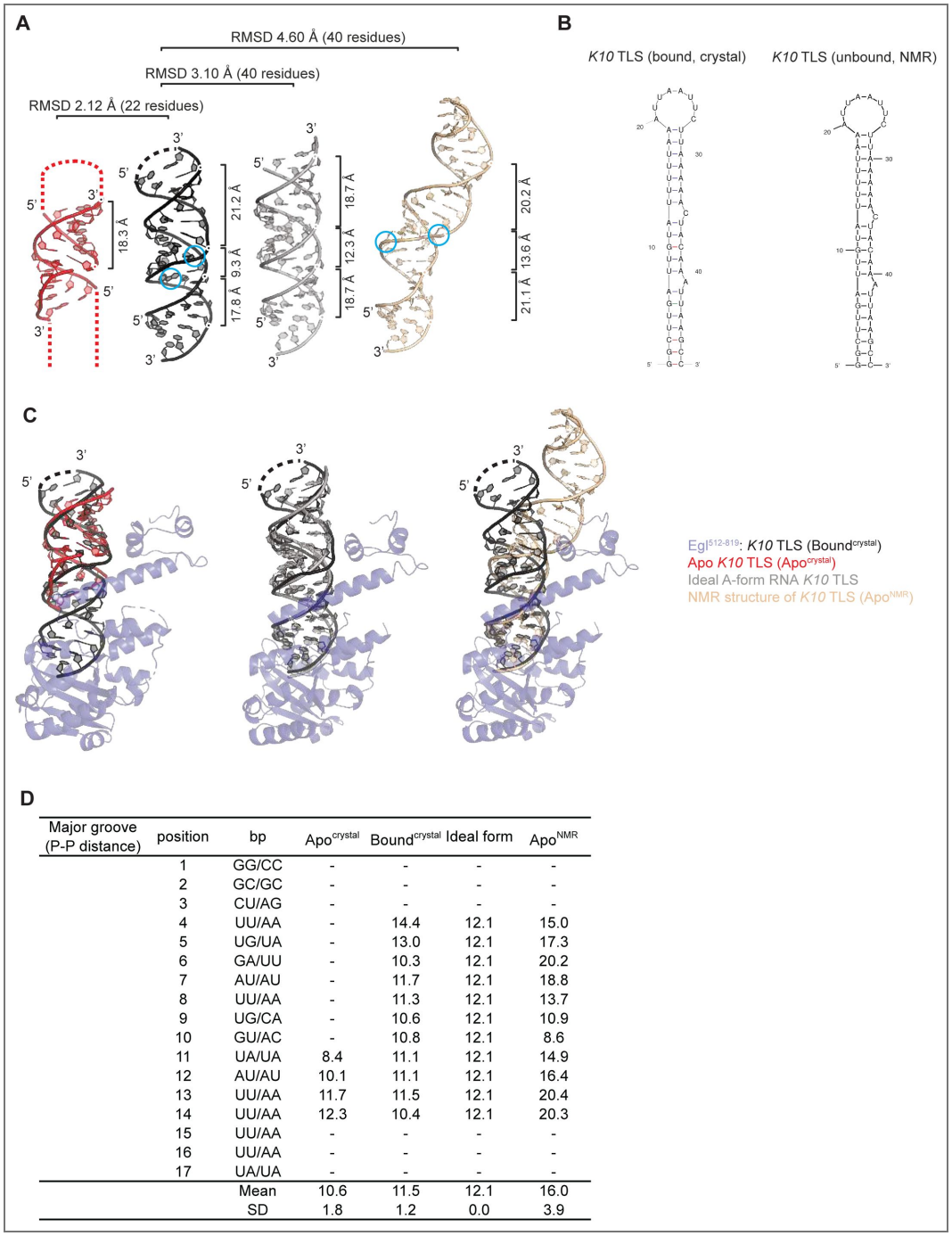

D

Major groove (P-P distance)	position	bp	Apo^{crystal}	Bound^{crystal}	Ideal form	Apo^{NMR}
	1	GG/CC	-	-	-	-
	2	GC/GC	-	-	-	-
	3	CU/AG	-	-	-	-
	4	UU/AA	-	14.4	12.1	15.0
	5	UG/UA	-	13.0	12.1	17.3
	6	GA/UU	-	10.3	12.1	20.2
	7	AU/AU	-	11.7	12.1	18.8
	8	UU/AA	-	11.3	12.1	13.7
	9	UG/CA	-	10.6	12.1	10.9
	10	GU/AC	-	10.8	12.1	8.6
	11	UA/UA	8.4	11.1	12.1	14.9
	12	AU/AU	10.1	11.1	12.1	16.4
	13	UU/AA	11.7	11.5	12.1	20.4
	14	UU/AA	12.3	10.4	12.1	20.3
	15	UU/AA	-	-	-	-
	16	UU/AA	-	-	-	-
	17	UA/UA	-	-	-	-
		Mean	10.6	11.5	12.1	16.0
		SD	1.8	1.2	0.0	3.9

Figure S3. Conformational changes of *K10* TLS in the complex and in isolation, related to Figure 3.

(A) From left to right: crystal structures of *K10* TLS (in red), of the Egl$^{512-819}$ bound *K10* TLS (in black), ideal A-form RNA *K10* TLS lacking the two bulges C35 and A41 (Δbulges) (in gray) and NMR solution structure of *K10* TLS (PDB ID.: 2KE6; Bullock et al. 2010; in gold) in a similar view. The width of major/minor grooves and RMSD are indicated. **(B)** Schematic representation of both Egl$^{512-819}$ bound *K10* TLS and NMR solution structure of *K10* TLS. **(C)** Structural alignments of the Egl$^{512-819}$ bound *K10* TLS with *K10* TLS (left), with an ideal A-form RNA *K10* TLS (Δbulges) (middle) and with the NMR solution structure of *K10* TLS. **(D)** *K10* TLS structural parameters calculated with w3DNA (Zheng et al., 2009). Major groove widths: direct P-P distances, not accounting for Van der Waals radii of the phosphate groups. Graphical illustrations of the parameters are reproduced from *http://x3dna.org* (Lu and Olson, 2003).

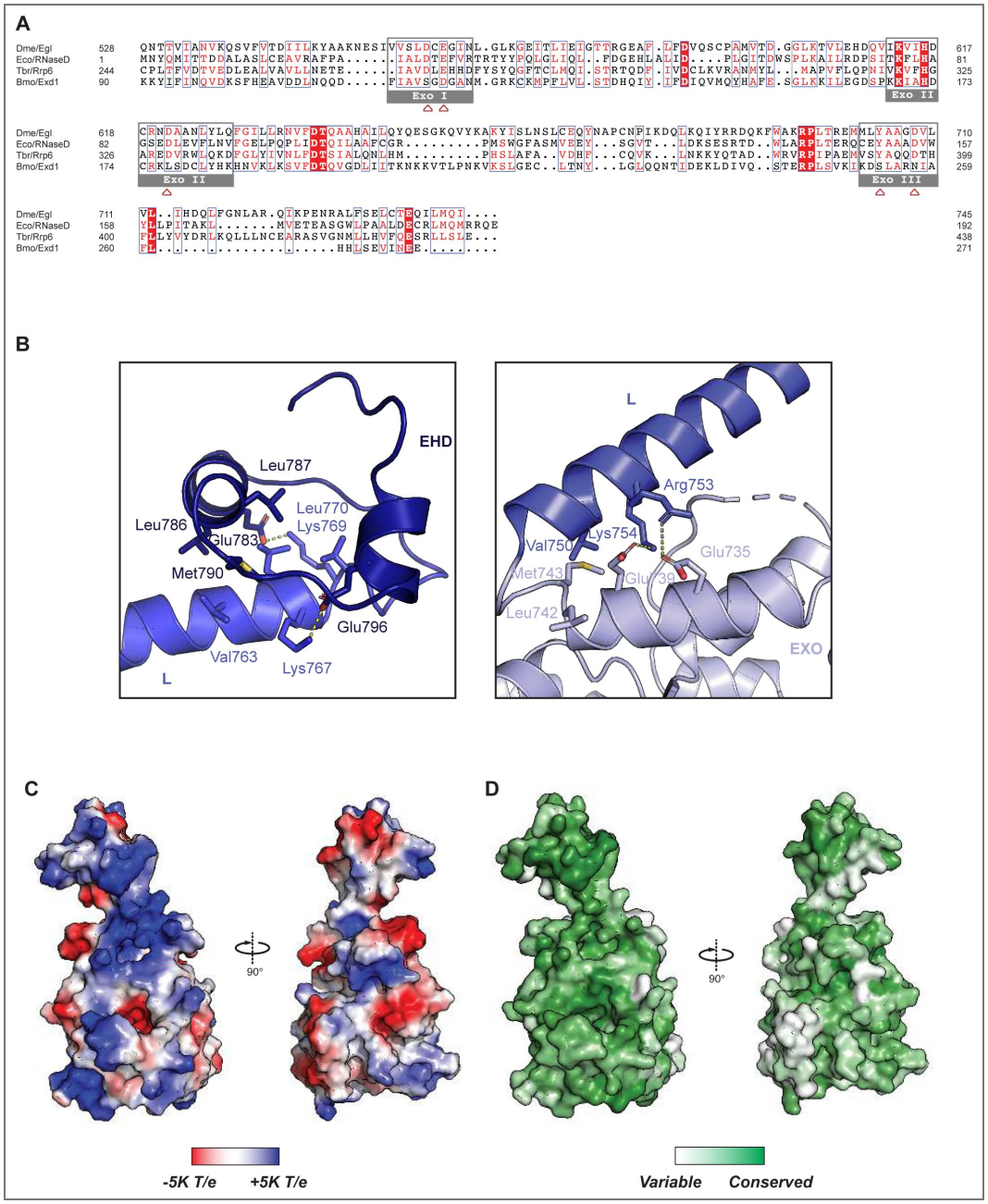

Figure S4. Alignment of Egl-related EXO domains, interdomain interaction of Egl$^{512-819}$ and *K10* RNA binds at positively charged and conserved residues on the surface of Egl$^{512-819}$, related to Figure 2 and 3.

(A) Sequence alignment of the EXO domains of *D. melanogaster* Egl (Egl_Dme), *E. coli* RNase D (RNaseD_Eco), *T. brucei* RRP6 (RRP6_Tbr) and *B. mori* EXO domain-containing 1 (Exd1_Bmo). Conserved residues are highlighted in red. Green boxes indicate exonuclease signature motifs, while signature catalytic residues are marked with △. The alignment was generated with MUSCLE (Edgar, 2004), visualized with ESPript (Robert and Gouet, 2014) and edited in Adobe Illustrator. The catalytic sites are marked by light gray boxes. **(B)** Interdomain interaction of Egl$^{512-819}$. (**C**-**D**) Surface representation of Egl in the same orientation as in **(C)** and rotated 90° along the *x* axis. In **(C)**, the surface is colored according to electrostatic potential, with positively charged residues in blue. In **(D)**, the surface is colored according to conservation, with a gradient from white to green indicating increasingly conserved residues. Conservation scores were calculated from the Egl sequences included in the multiple sequence alignment shown in Figure S1A, by using ConSurf (Ashkenazy et al., 2016).

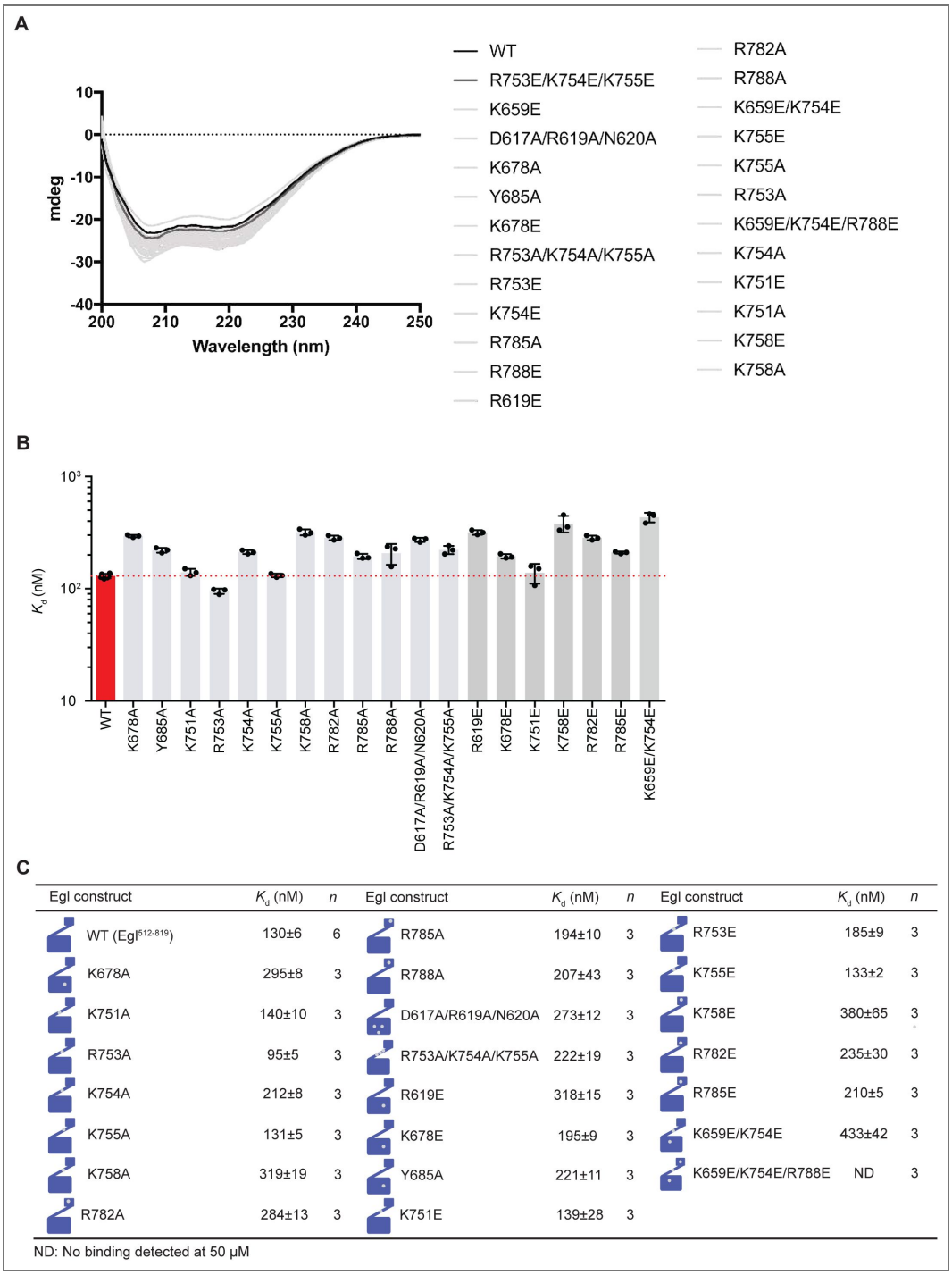

C

Egl construct	K_d (nM)	*n*	Egl construct	K_d (nM)	*n*	Egl construct	K_d (nM)	*n*
WT ($Egl^{512-819}$)	130±6	6	R785A	194±10	3	R753E	185±9	3
K678A	295±8	3	R788A	207±43	3	K755E	133±2	3
K751A	140±10	3	D617A/R619A/N620A	273±12	3	K758E	380±65	3
R753A	95±5	3	R753A/K754A/K755A	222±19	3	R782E	235±30	3
K754A	212±8	3	R619E	318±15	3	R785E	210±5	3
K755A	131±5	3	K678E	195±9	3	K659E/K754E	433±42	3
K758A	319±19	3	Y685A	221±11	3	K659E/K754E/R788E	ND	3
R782A	284±13	3	K751E	139±28	3			

ND: No binding detected at 50 μM

Figure S5. Binding affinity of Egl alanine mutants to *K10* TLS and Circular Dichroism spectra of Egl mutants used in this study, related to Figure 4.

(A) Circular Dichroism (CD) spectra of recombinantly purified Egl mutants used in FA. Wavelength scans are averages of five scans between 200 nm and 250 nm collected at 20°C in a quartz cuvette with a 1-mm path length with 0.2 mg/ml protein in buffer (20 mM Tris-HCl, pH 7.5, 300 mM NaCl, 10% glycerol, 1 mM DTT). Wavelength scans are shown as solid curves with Egl WT colored in black, the R753E/K754E/K755E triple mutant in dark gray, and the other mutants in light gray. **(B)** Column graph with mean K_d shown as bars, standard deviation as black error bars and individual Kd values as black dots. **(C)** K_d values between Egl alanine mutants and *K10* TLS are shown in the table.

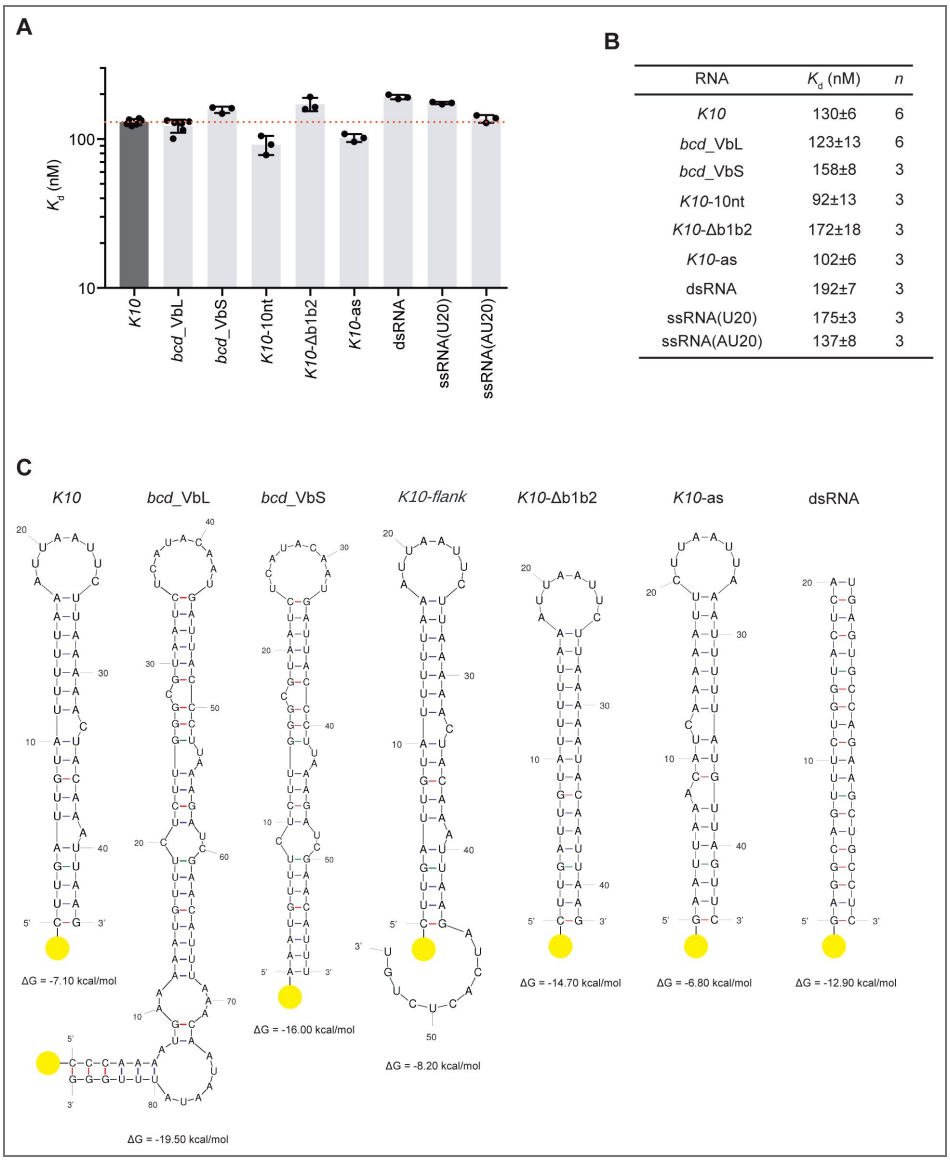

RNA	K_d (nM)	*n*
K10	130±6	6
*bcd*_VbL	123±13	6
*bcd*_VbS	158±8	3
K10-10nt	92±13	3
K10-Δb1b2	172±18	3
K10-as	102±6	3
dsRNA	192±7	3
ssRNA(U20)	175±3	3
ssRNA(AU20)	137±8	3

Figure S6. Binding affinity of Egl$^{512-819}$ to RNA variants, related to Figure 5.

(A) and **(B)** K_d values were determined by FA. 5'-FAM-labeled RNA variants were incubated with increasing concentrations of Egl$^{512-819}$ and the data were fitted to the Hill equation to obtain the K_d. Data are represented as mean ± SD. **(A)** Column graph with mean K_d was shown as bars, standard deviation as black error bars and individual K_d values as black dots. **(B)** K_d values between Egl$^{512-819}$ and RNA variants are shown in the table. Data are represented as mean ± SD. **(C)** Secondary structures of RNA variants used for direct binding assay. **(D)** Secondary structures of RNA variants used in competition assay. Secondary structures of RNA variants were generated with mFold (Zuker 2003).

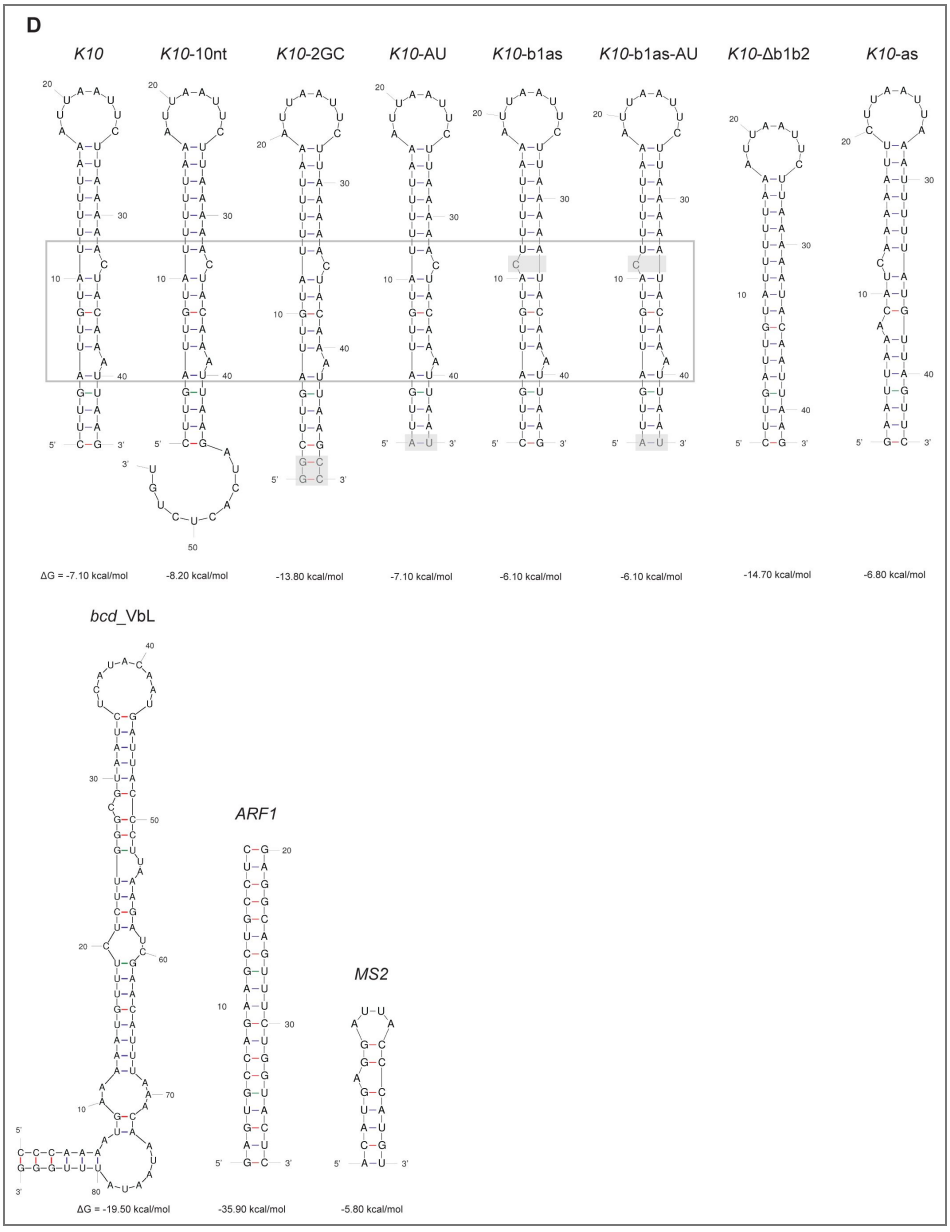

Figure S6. (continued)

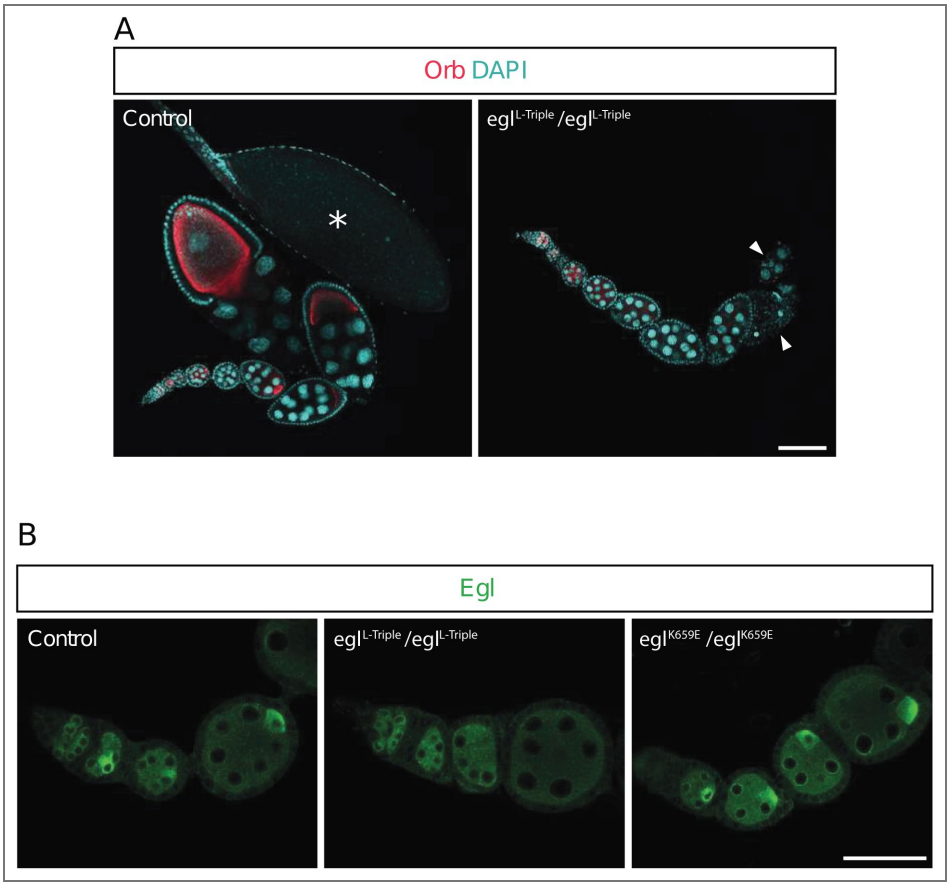

Figure S7. Additional characterisation of *egl* mutations in *Drosophila*, related to Figure 6.

(A) Female flies homozygous for the *L-Triple* mutation fail to produce mature oocytes (labelled in the control by an asterisk). In the control ovariole, developing oocytes within syncytial egg chambers are visualised by staining with an anti-Orb antibody (red). DNA is labelled with DAPI (cyan). In the absence of oocyte differentiation, mutant egg chambers eventually degenerate (arrowheads), which is consistent with previous observations in *egl* null mutants(Mach and Lehmann, 1997). Scale bar, 100 µm. Images are representative of > 200 ovarioles examined per genotype. Control genotype is *PR29/+*, which has indistinguishable oocyte development from the wild-type. **(B)** The mutations in *egl* that impair RNA binding do not prevent protein expression. Images are of germaria and early egg chambers. Note that Egl (green) accumulates in the oocyte in control egg chambers by microtubule-based transport(Mach and Lehmann, 1997). This accumulation is also seen in *K659E/K659E* egg chambers, which have no overt defects in oocyte differentiation (Fig. 6B). In contrast, homozygous *L-Triple* fail to differentiate an oocyte (Fig. 6A) and therefore do not accumulate Egl asymmetrically in the egg chamber. Thus, for this genotype, protein levels in the rest of the egg chamber should be compared to control. Control is wild type (w^{1118}). Scale bar = 50 µm. Images are representative of > 75 ovarioles imaged per genotype.

Data availability

The coordinates and structure factors have been deposited in the Macromolecular Structure Database of European Bioinformatic Institute (EBI) with ID code 9UJU, 9UJY and 9UUG for Egl512-819-K10 TLS complex, MBP-(GSAM)-L-EHD and K10-TR.

Acknowledgements

We wish to thank the MPI-Tuebingen Crystallization Facility. We also thank the staff at the Swiss Light Source synchrotron for assistance during data collection, Claire Basquin for assistance with MALLS measurements and Stefanie Wachter for initial stages of the project. We thank G. Jékely and A. Cook for discussion and critical reading of the manuscript. This project has received funding from the European Research Council under the European Union's Seventh Framework Programme (FP7/2007-2013), ERC grant agreement n° 310957 and the Deutsche Forschungsgemeinschaft (FOR2333 to F.B.). L.J. and S.L.B. are supported by the MRC (file reference number MC_U105178790). Z.H is supported by A*STAR, National Medical Research Council (NMRC; reference number OFYIRG23jul-0062).

Additional information

Author Contributions

Biochemical, biophysical and crystallization work was done by Z.H. and J.M.; *Drosophila* work was done by L.J.; F.B. supervised the project. All authors wrote the paper.

Funding

Funder	Grant reference number	Author
MOH | National Medical Research Council (NMRC)	OFYIRG23jul-0062	Zebin Hong

Author ORCID iDs

Zebin Hong: https://orcid.org/0000-0002-8358-1474

References

Ashkenazy H., Abadi S., Martz E., Chay O., Mayrose I., Pupko T., Ben-Tal N (2016) ConSurf 2016: an improved methodology to estimate and visualize evolutionary conservation in macromolecules. *Nucleic Acids Res* **44**:W344-350 https://doi.org/10.1093/nar/gkw408 | PubMed

Barbosa R.L., Legrand P., Wien F., Pineau B., Thompson A., Guimarães B.G (2014) RRP6 from Trypanosoma brucei: crystal structure of the catalytic domain, association with EAP3 and activity towards structured and non-structured RNA substrates. *PLoS One* **9**:e89138 https://doi.org/10.1371/journal.pone.0089138 | PubMed

Besse F., Ephrussi A (2008) Translational control of localized mRNAs: restricting protein synthesis in space and time. *Nat Rev Mol Cell Biol* **9**:971-980 https://doi.org/10.1038/nrm2548 | PubMed

Bullock S.L., Ish-Horowicz D (2001) Conserved signals and machinery for RNA transport in Drosophila oogenesis and embryogenesis. *Nature* **414**:611-616 https://doi.org/10.1038/414611a | PubMed

Bullock S.L., Ringel I., Ish-Horowicz D., Lukavsky P.J (2010) A'-form RNA helices are required for cytoplasmic mRNA transport in Drosophila. *Nat Struct Mol Biol* **17**:703-709 https://doi.org/10.1038/nsmb.1813 | PubMed

Bullock S.L., Zicha D., Ish-Horowicz D (2003) The Drosophila hairy RNA localization signal modulates the kinetics of cytoplasmic mRNA transport. *EMBO J* **22**:2484-2494 https://doi.org/10.1093/emboj/cdg230 | PubMed

Carpenter A.T (1994) Egalitarian and the choice of cell fates in Drosophila melanogaster oogenesis. *Ciba Found Symp* **182**:223-246 https://doi.org/10.1002/9780470514573.ch13 | PubMed

Cheung H.K., Serano T.L., Cohen R.S (1992) Evidence for a highly selective RNA transport system and its role in establishing the dorsoventral axis of the Drosophila egg. *Development* **114**:653-661 https://doi.org/10.1242/dev.114.3.653 | PubMed

Chojnowski G., Waleń T., Piątkowski P., Potrzebowski W., Bujnicki J.M (2015) Brickworx builds recurrent RNA and DNA structural motifs into medium- and low-resolution electron-density maps. *Acta Crystallogr D Biol Crystallogr* **71**:697-705 https://doi.org/10.1107/s1399004715000383 | PubMed

Claussen M., Suter B (2005) BicD-dependent localization processes: from Drosophilia development to human cell biology. *Ann Anat* **187**:539-553 https://doi.org/10.1016/j.aanat.2005.07.004 | PubMed

Cohen R.S., Zhang S., Dollar G.L (2005) The positional, structural, and sequence requirements of the Drosophila TLS RNA localization element. *RNA* **11**:1017-1029 https://doi.org/10.1261/rna.7218905 | PubMed

Collins K.A., Unruh J.R., Slaughter B.D., Yu Z., Lake C.M., Nielsen R.J., Box K.S., Miller D.E., Blumenstiel J.P., Perera A.G., *et al.* (2014) Corolla is a novel protein that contributes to the architecture of the synaptonemal complex of Drosophila. *Genetics* **198**:219-228 https://doi.org/10.1534/genetics.114.165290 | PubMed

Diebold M.-L., Fribourg S., Koch M., Metzger T., Romier C (2011) Deciphering correct strategies for multiprotein complex assembly by co-expression: application to complexes as large as the histone octamer. *J Struct Biol* **175**:178-188 https://doi.org/10.1016/j.jsb.2011.02.001 | PubMed

Dienstbier M., Boehl F., Li X., Bullock S.L (2009) Egalitarian is a selective RNA-binding protein linking mRNA localization signals to the dynein motor. *Genes Dev* **23**:1546-1558 https://doi.org/10.1101/gad.531009 | PubMed

dos Santos G., Simmonds A.J., Krause H.M. (2008) A stem-loop structure in the wingless transcript defines a consensus motif for apical RNA transport. *Development* **135**:133-143 https://doi.org/10.1242/dev.014068 | PubMed

Edgar R.C (2004) MUSCLE: a multiple sequence alignment method with reduced time and space complexity. *BMC Bioinformatics* **5**:113 https://doi.org/10.1186/1471-2105-5-113 | PubMed

Emsley P., Lohkamp B., Scott W.G., Cowtan K (2010) Features and development of Coot. *Acta Crystallogr D Biol Crystallogr* **66**:486-501 https://doi.org/10.1107/s0907444910007493 | PubMed

Ennifar E., Yusupov M., Walter P., Marquet R., Ehresmann B., Ehresmann C., Dumas P (1999) The crystal structure of the dimerization initiation site of genomic HIV-1 RNA reveals an extended duplex with two adenine bulges. *Structure* **7**:1439-1449 https://doi.org/10.1016/s0969-2126(00)80033-7 | PubMed

Herbert A.L., Fu M.-M., Drerup C.M., Gray R.S., Harty B.L., Ackerman S.D., O'Reilly-Pol T., Johnson S.L., Nechiporuk A.V., Barres B.A., *et al.* (2017) Dynein/dynactin is necessary for anterograde transport of Mbp mRNA in oligodendrocytes and for myelination in vivo. *Proc Natl Acad Sci U S A* **114**:E9153-E9162 https://doi.org/10.1073/pnas.1711088114 | PubMed

Hermann T., Patel D.J (2000) RNA bulges as architectural and recognition motifs. *Structure* **8**:R47-54 https://doi.org/10.1016/s0969-2126(00)00110-6 | PubMed

Ho B.X., Pang J.K.S., Chen Y., Loh Y.-H., An O., Yang H.H., Seshachalam V.P., Koh J.L.Y., Chan W.-K., Ng S.Y., *et al.* (2022) Robust generation of human-chambered cardiac organoids from pluripotent stem cells for improved modelling of cardiovascular diseases. *Stem Cell Res Ther* **13**:529 https://doi.org/10.1186/s13287-022-03215-1 | PubMed

Holm L., Laakso L.M (2016) Dali server update. *Nucleic Acids Res* **44**:W351-355 https://doi.org/10.1093/nar/gkw357 | PubMed

Holt C.E., Bullock S.L (2009) Subcellular mRNA localization in animal cells and why it matters. *Science* **326**:1212-1216 https://doi.org/10.1126/science.1176488 | PubMed

Hoogenraad C.C., Akhmanova A., Howell S.A., Dortland B.R., De Zeeuw C.I., Willemsen R., Visser P., Grosveld F., Galjart N. (2001) Mammalian Golgi-associated Bicaudal-D2 functions in the dynein-dynactin pathway by interacting with these complexes. *EMBO J* **20**:4041-4054 https://doi.org/10.1093/emboj/20.15.4041 | PubMed

Hughes J.R., Bullock S.L., Ish-Horowicz D (2004) Inscuteable mRNA localization is dynein-dependent and regulates apicobasal polarity and spindle length in Drosophila neuroblasts. *Curr Biol* **14**:1950-1956 https://doi.org/10.1016/j.cub.2004.10.022 | PubMed

Kabsch W (2010) XDS. *Acta Crystallogr D Biol Crystallogr* **66**:125-132 https://doi.org/10.1107/s0907444909047337 | PubMed

Kim Y.K., Furic L., Desgroseillers L., Maquat L.E (2005) Mammalian Staufen1 recruits Upf1 to specific mRNA 3'UTRs so as to elicit mRNA decay. *Cell* **120**:195-208 https://doi.org/10.1016/j.cell.2004.11.050 | PubMed

Krissinel E., Henrick K (2007) Inference of macromolecular assemblies from crystalline state. *J Mol Biol* **372**:774-797 https://doi.org/10.1016/j.jmb.2007.05.022 | PubMed

Lantz V., Chang J.S., Horabin J.I., Bopp D., Schedl P (1994) The Drosophila orb RNA-binding protein is required for the formation of the egg chamber and establishment of polarity. *Genes Dev* **8**:598-613 https://doi.org/10.1101/gad.8.5.598 | PubMed

Lantz V., Schedl P (1994) Multiple cis-acting targeting sequences are required for orb mRNA localization during Drosophila oogenesis. *Mol Cell Biol* **14**:2235-2242 https://doi.org/10.1128/mcb.14.4.2235-2242.1994 | PubMed

Lazzaretti D., Veith K., Kramer K., Basquin C., Urlaub H., Irion U., Bono F (2016) The bicoid mRNA localization factor Exuperantia is an RNA-binding pseudonuclease. *Nat Struct Mol Biol* **23**:705-713 https://doi.org/10.1038/nsmb.3254 | PubMed

Li Z., Pandit S., Deutscher M.P (1998) 3' exoribonucleolytic trimming is a common feature of the maturation of small, stable RNAs in Escherichia coli. *Proc Natl Acad Sci U S A* **95**:2856-2861 https://doi.org/10.1073/pnas.95.6.2856 | PubMed

Liu Y., Salter H.K., Holding A.N., Johnson C.M., Stephens E., Lukavsky P.J., Walshaw J., Bullock S.L (2013) Bicaudal-D uses a parallel, homodimeric coiled coil with heterotypic registry to coordinate recruitment of cargos to dynein. *Genes Dev* **27**:1233-1246 https://doi.org/10.1101/gad.212381.112 | PubMed

Macdonald P.M., Kerr K (1998) Mutational analysis of an RNA recognition element that mediates localization of bicoid mRNA. *Mol Cell Biol* **18**:3788-3795 https://doi.org/10.1128/mcb.18.7.3788 | PubMed

Mach J.M., Lehmann R (1997) An Egalitarian-BicaudalD complex is essential for oocyte specification and axis determination in Drosophila. *Genes Dev* **11**:423-435 https://doi.org/10.1101/gad.11.4.423 | PubMed

Martin K.C., Ephrussi A (2009) mRNA localization: gene expression in the spatial dimension. *Cell* **136**:719-730 https://doi.org/10.1016/j.cell.2009.01.044 | PubMed

McClintock M.A., Dix C.I., Johnson C.M., McLaughlin S.H., Maizels R.J., Hoang H.T., Bullock S.L (2018) RNA-directed activation of cytoplasmic dynein-1 in reconstituted transport RNPs. *eLife* **7**:e36312 https://doi.org/10.7554/eLife.36312 | PubMed

McCoy A.J., Grosse-Kunstleve R.W., Adams P.D., Winn M.D., Storoni L.C., Read R.J (2007) Phaser crystallographic software. *J Appl Crystallogr* **40**:658-674 https://doi.org/10.1107/s0021889807021206 | PubMed

Navarro C., Puthalakath H., Adams J.M., Strasser A., Lehmann R (2004) Egalitarian binds dynein light chain to establish oocyte polarity and maintain oocyte fate. *Nat Cell Biol* **6**:427-435 https://doi.org/10.1038/ncb1122 | PubMed

Oh J., Baksa K., Steward R (2000) Functional domains of the Drosophila bicaudal-D protein. *Genetics* **154**:713-724 https://doi.org/10.1093/genetics/154.2.713 | PubMed

Page S.L., Hawley R.S (2001) c(3)G encodes a Drosophila synaptonemal complex protein. *Genes Dev* **15**:3130-3143 https://doi.org/10.1101/gad.935001 | PubMed

Port F., Bullock S.L (2016) Creating Heritable Mutations in Drosophila with CRISPR-Cas9. *Methods Mol Biol* **1478**:145-160 https://doi.org/10.1007/978-1-4939-6371-3_7 | PubMed

Port F., Chen H.-M., Lee T., Bullock S.L (2014) Optimized CRISPR/Cas tools for efficient germline and somatic genome engineering in Drosophila. *Proc Natl Acad Sci U S A* **111**:E2967-2976 https://doi.org/10.1073/pnas.1405500111 | PubMed

Quiocho F.A., Spurlino J.C., Rodseth L.E (1997) Extensive features of tight oligosaccharide binding revealed in high-resolution structures of the maltodextrin transport/chemosensory receptor. *Structure* **5**:997-1015 https://doi.org/10.1016/s0969-2126(97)00253-0 | PubMed

Serano T.L., Cohen R.S (1995) A small predicted stem-loop structure mediates oocyte localization of Drosophila K10 mRNA. *Development* **121**:3809-3818 https://doi.org/10.1242/dev.121.11.3809 | PubMed

Sladewski T.E., Billington N., Ali M.Y., Bookwalter C.S., Lu H., Krementsova E.B., Schroer T.A., Trybus K.M (2018) Recruitment of two dyneins to an mRNA-dependent Bicaudal D transport complex. *eLife* **7**:e36306 https://doi.org/10.7554/eLife.36306 | PubMed

Snee M.J., Arn E.A., Bullock S.L., Macdonald P.M (2005) Recognition of the bcd mRNA localization signal in Drosophila embryos and ovaries. *Mol Cell Biol* **25**:1501-1510 https://doi.org/10.1128/mcb.25.4.1501-1510.2005 | PubMed

St Johnston D. (2005) Moving messages: the intracellular localization of mRNAs. *Nat Rev Mol Cell Biol* **6**:363-375 https://doi.org/10.1038/nrm1643 | PubMed

St Johnston D. (1995) The intracellular localization of messenger RNAs. *Cell* **81**:161-170 https://doi.org/10.1016/0092-8674(95)90324-0 | PubMed

Sutton M.A., Schuman E.M (2006) Dendritic protein synthesis, synaptic plasticity, and memory. *Cell* **127**:49-58 https://doi.org/10.1016/j.cell.2006.09.014 | PubMed

Tekotte H., Davis I (2002) Intracellular mRNA localization: motors move messages. *Trends Genet* **18**:636-642 https://doi.org/10.1016/s0168-9525(02)02819-6 | PubMed

Terwilliger T.C., DiMaio F., Read R.J., Baker D., Bunkóczi G., Adams P.D., Grosse-Kunstleve R.W., Afonine P.V., Echols N (2012) phenix.mr_rosetta: molecular replacement and model rebuilding with Phenix and Rosetta. *Journal of Structural and Functional Genomics* **13**:81 https://doi.org/10.1007/s10969-012-9129-3 | PubMed

Theurkauf W.E., Alberts B.M., Jan Y.N., Jongens T.A (1993) A central role for microtubules in the differentiation of Drosophila oocytes. *Development* **118**:1169-1180 https://doi.org/10.1242/dev.118.4.1169 | PubMed

Trovisco V., Belaya K., Nashchekin D., Irion U., Sirinakis G., Butler R., Lee J.J., Gavis E.R., St Johnston D (2016) bicoid mRNA localises to the Drosophila oocyte anterior by random Dynein-mediated transport and anchoring. *eLife* **5**:e17537 https://doi.org/10.7554/eLife.17537 | PubMed

Vagin A.A., Steiner R.A., Lebedev A.A., Potterton L., McNicholas S., Long F., Murshudov G.N (2004) REFMAC5 dictionary: organization of prior chemical knowledge and guidelines for its use. *Acta Crystallogr D Biol Crystallogr* **60**:2184-2195 https://doi.org/10.1107/s0907444904023510 | PubMed

Van De Bor V., Hartswood E., Jones C., Finnegan D., Davis I. (2005) gurken and the I factor retrotransposon RNAs share common localization signals and machinery. *Dev Cell* **9**:51-62 https://doi.org/10.1016/j.devcel.2005.04.012 | PubMed

Vazquez-Pianzola P., Schaller B., Colombo M., Beuchle D., Neuenschwander S., Marcil A., Bruggmann R., Suter B (2017) The mRNA transportome of the BicD/Egl transport machinery. *RNA Biol* **14**:73-89 https://doi.org/10.1080/15476286.2016.1251542 | PubMed

Waterhouse A.M., Procter J.B., Martin D.M.A., Clamp M., Barton G.J. (2009) Jalview Version 2--a multiple sequence alignment editor and analysis workbench. *Bioinformatics* **25**:1189-1191 https://doi.org/10.1093/bioinformatics/btp033 | PubMed

Yang J., Zhang Y (2015) Protein Structure and Function Prediction Using I-TASSER. *Curr Protoc Bioinformatics* **52**:5.8.1-5.8.15 https://doi.org/10.1002/0471250953.bi0508s52 | PubMed

Yang Z., Chen K.-M., Pandey R.R., Homolka D., Reuter M., Janeiro B.K.R., Sachidanandam R., Fauvarque M.-O., McCarthy A.A., Pillai R.S (2016) PIWI Slicing and EXD1 Drive Biogenesis of Nuclear piRNAs from Cytosolic Targets of the Mouse piRNA Pathway. *Mol Cell* **61**:138-152 https://doi.org/10.1016/j.molcel.2015.11.009 | PubMed

Zuker M (2003) Mfold web server for nucleic acid folding and hybridization prediction. *Nucleic Acids Res* **31**:3406-3415 https://doi.org/10.1093/nar/gkg595 | PubMed

Peer reviews

Reviewer #1 (Public review):

Summary:

The authors sought to define the molecular mechanism by which the adaptor protein Egalitarian (Egl) recognizes and binds specific mRNA localization signals -- in particular, the K10 transport and localization signal (TLS) -- to initiate dynein-based transport in Drosophila. In doing so, they identified the minimal Egl domains required for RNA binding, determined the atomistic structure of the Egl-RNA complex, and explored the recognition mechanism (shape vs. structure). They furthermore performed in vivo functional validation using CRISPR-mediated genome editing in Drosophila that showed that the identified binding residues are biologically essential.

Strengths:

The authors provided a detailed crystal structure of the Egl-RNA complex at high resolution. In particular, they used a MBP-fusion crystallization driver to be able to resolve the flexible C-terminal domain of Egl (EHD). The authors' use of an integrative approach combining X-ray crystallography with binding assays and in vivo functional validation provides compelling evidence for their claims.

The work provides a detailed interaction mapping that identifies the protein residues responsible for the electrostatic interaction with the RNA. In doing so, the work explains how Egl can recognize diverse RNA sequences by demonstrating that Egl binds primarily to the phosphate backbone and specific structural bulges, providing a plausible model for how one protein can recognize many different localization signals that share little sequence similarity.

Weaknesses:

Discrepancy in the stoichiometric Egl-to-RNA ratio (the structural data in the paper indicate a 1:1 ratio, whereas previous single-molecule transport studies suggest a 2:1 ratio) remains unanswered, with the likely explanation that the truncated version of the protein might not capture the full (native) assembly. While the authors acknowledge this in the Discussion, the paper would benefit from this issue being raised earlier, already in the Results section. Moreover, there is a notable omission of a recent preprint on a very similar topic [*https://www.biorxiv.org/content/10.1101/2025.08.02.668268v1.full]*.

In vitro, Egl shows a relatively high affinity for non-target RNAs such as the MS2 loop, whereas it is highly selective in vivo. Is it possible that other cofactors are required for the high-fidelity sorting not present in the study? Testing binding in the presence of co-factors (BicD or Dlc) could indicate whether they increase the specificity for target RNAs over non-target ones.

Including a more diverse set of size-matched RNA controls would have significantly strengthened the paper's claims regarding specificity. Using RNAs that mimic K10 TLS would

have provided a more rigorous test of the shape-recognition by Egl - using, for instance, decoy RNAs of the same length but with differently positioned bulges (or no bulges at all) or testing other known localization signals (like bicoid or hairy) of similar length.

Appraisal of aims:

The authors successfully determined the crystal structure of the Egl-RNA complex, identifying a modular binding surface composed of the EXO domain, a helical linker, and the EHD. They effectively demonstrated that Egl uses a combination of shape-specific recognition (targeting RNA bulges) and sequence-specific interactions (bonding with specific bases), and confirmed the biological necessity of these findings by showing that mutating the identified residues in living flies leads to infertility and oocyte differentiation defects. These results provide robust evidence for the authors' claims that they have defined a minimal RNA localization signal. In particular, the correlation between the L-Triple mutation's binding defect and its total sterility in flies provides proof that the identified binding surface is the functional one. While the 1:1 stoichiometry remains a point for further investigation, the authors transparently address that full-length transport may require a 2:1 assembly, suggesting their structure represents the fundamental building block of that larger complex.

Impact of the work on the field:

This study provides a high-resolution picture of how a dynein adaptor recognizes its cargo. It moves the field from predictive models to atomic-level certainty, setting a benchmark for studying other similar transport complexes. By proving that Egl recognizes RNA shape (bulges) as much as sequence, the work changes the outlook on the search for localization signals in other genomes, moving beyond simple sequence motifs to 3D structural signatures. The coordinates deposited in the EBI (IDs: 9UJU, 9UJY, 9UUG) provide a resource for the modelling of higher-order transport complexes. The identification of specific residues (e.g., the L-Triple) provides the community with tools to disrupt RNA transport in Drosophila without destroying the entire protein, allowing for more nuanced studies of development.

https://doi.org/10.7554/eLife.110988.1.sa2

Reviewer #2 (Public review):

Summary:

Hong et. al. aimed to elucidate the structural basis of the Egalitarian recognition of the K10 mRNA. Using X-ray crystallography and several biochemical, biophysical, and cellular techniques, they were able to shed light on the formation, stability, and basis of interaction of the complex. The authors successfully accomplished their goal.

Strengths:

The experiments are well-performed and convincing. The manuscript is well-written.

Weaknesses:

(1) Some statistical analysis would improve the manuscript. In particular, the manuscript has several results that are based on comparisons, such as Kd. Adding p-values for significance is recommended, and this would improve the treatment of data.

(2) When showing interactions (dotted lines) in structural figures, adding the distance would be useful and is recommended.

(3) Additional SI Figure. It would enrich the manuscript to have the composite simulated annealing-omit 2|Fo| - |Fc | electron density maps for the structures contoured at a given

sigma, superimposed on the final refined model. This would represent how well the data fits into the model.

https://doi.org/10.7554/eLife.110988.1.sa1

Author response:

We would like to thank the editors and the reviewers for their thoughtful and constructive assessment of our manuscript. We appreciate the reviewers' positive recognition of our research and their thoughtful assessment of our data.

In the upcoming revision, we will incorporate rigorous statistical analysis (p-values) for our binding assays, optimize the structural figures and summary tables for better clarity, and discuss the recent preprint paper alongside the nuances of Egl-BicD stoichiometry. Regarding the suggestion for CLIP-seq, we agree that a global analysis would be a valuable extension of this work. However, as our lab's core expertise is in structural biology, and the in vivo functional studies in this manuscript were conducted through a collaboration to validate our structural findings, we feel that such a large-scale genomic study falls beyond the scope of the current structural report.

https://doi.org/10.7554/eLife.110988.1.sa0